Photonic heat engines at thermodynamic limits

Zunaid Omair

Electrical Engineering and Computer Sciences
University of California, Berkeley

Technical Report No. UCB/EECS-2023-21
http://www2.eecs.berkeley.edu/Pubs/TechRpts/2023/EECS-2023-21.html

May 1, 2023

Photonic Heat Engines at Thermodynamic Limits

By

Zunaid Omair

A dissertation submitted in partial satisfaction of the
requirements for the degree of
Doctor of Philosophy
In
Engineering – Electrical Engineering and Computer Sciences
in the
Graduate Division
of the
University of California, Berkeley

Committee in charge:
Professor Eli Yablonovitch, Chair
Professor Boubacar Kante
Professor Ming Wu
Professor Per F Peterson
Spring 2021

Abstract
Photonic Heat Engines at Thermodynamic Limits
by

Zunaid Omair

Doctor of Philosophy in Electrical Engineering and Computer Sciences

University of California, Berkeley

Professor Eli Yablonovitch, Chair

In thermophotovoltaic energy conversion, photovoltaic cells convert thermal radiation from a local emitter to electricity. The key is to find a way to exploit the great majority of low-energy thermal photons that would otherwise be unusable in a photovoltaic system. A highly reflective rear mirror can serendipitously boost the voltage, and regenerate the low-energy photons. Based on this concept, we demonstrate a 29.1% heat-to-electricity power conversion efficiency for thermophotovoltaics. We identify broadband mirrors as a major parameter to achieve thermophotovoltaic efficiency>50%. We show the challenges towards designing broadband mirrors and demonstrate an electromagnetic inverse-design approach based on Fresnel propagation. Finally, we demonstrate mirrors with >99% reflectivity over 3-octaves of frequency bandwidth. This new class of mirrors can make photonic heat engines based on thermophotovoltaics competitive with internal combustion engines.

Additionally, for record-breaking solar cells the external luminescence efficiency is decisive in determining the open-circuit voltage, $V_{oc}=V_{oc\text{-}ideal} -kT|\ln\{\eta_{ext}\}|$. External luminescence efficiency, η_{ext}, has produced all the record solar cells in the past 10 years. On the other hand, for poor luminescent materials, the external luminescence is far less decisive than the internal luminescence efficiency, $\eta_{int.}$. Most solar cells, including the important case of Silicon, luminesce very poorly. We express the open circuit voltage in terms of η_{int}, that provides the correct V_{oc} for poor luminescent materials. We show how the internal luminescence efficiency affects the open-circuit voltage. We identify the minimum internal luminescence needed to further improve open-circuit voltage through good external luminescence.

Table of Contents

Acknowledgements

The present work was financially supported by the Department of Energy (DOE) "Light-Material Interactions in Energy Conversion" Energy Frontier Research Center under Grant DE-SC0001293, DOE "Photonics at Thermodynamic Limit" Energy Frontier Research Center under Grant DE-SC00019140, and Eltoukhy East-West Gateway fellowship at International House, UC Berkeley. The author was emotionally supported by Dani and Pumbi.

1. Regenerative Thermophotovoltaics: Theory

Photovoltaic devices generate electricity from thermal radiation[1,2,3,4,5,6]. In thermophotovoltaic energy conversion, first described[7] in 1956, photovoltaic cells convert thermal radiation from a local emitter to electricity. The key is to find a way to exploit the great majority of low-energy thermal photons that would otherwise be unusable in a photovoltaic system.

Most effort in this regard has been directed towards engineering the hot emitter, making it spectrally selective such that it suppresses the emission of low-energy photons[8,9]. The spectral emissivity of the thermal source is tailored to the absorption edge of the photovoltaic cell[10,11], as illustrated in Fig. 1(a). The spectral filter has been implemented by photonic crystals[12,13,14,15,16,17], metamaterials[18,19,20,21,22] as well as rare-earth oxides[23,24].

We present a different approach. All new record-breaking solar cells now include a rear mirror to assist in the extraction[25] of band-edge luminescence from the photovoltaic cell. For high-quality photovoltaic materials, the rate of internal photon generation is high. However, in devices with poor photon management, this is typically quenched by a poor reflecting electrode in the back of the device. When a highly reflective mirror is inserted instead, a bright internal photon gas develops, maximizing the observed external luminescence flux, and producing a large carrier concentration. This provides a voltage boost of ~0.1Volts at the open circuit[26]. Indeed, the development of a highly reflective rear mirror has been the main driver of recent efficiency records in solar photovoltaics[27,28,29].

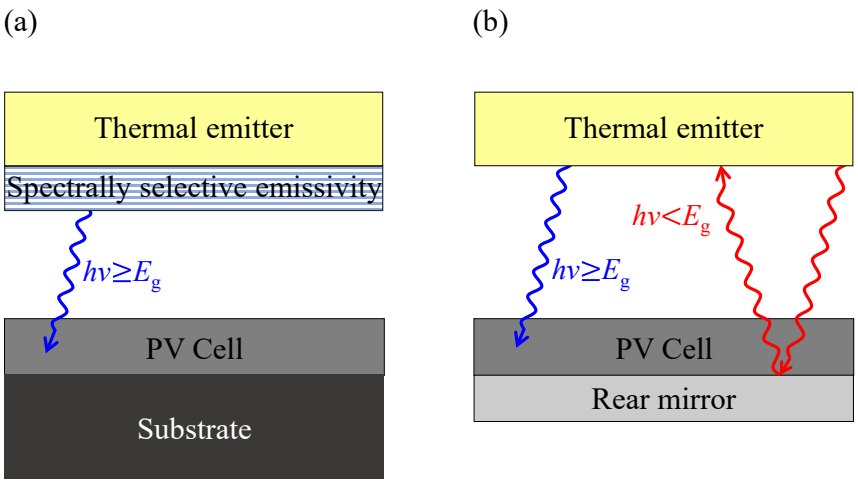

Figure 1. Increasing the efficiency of thermophotovoltaics by managing the low energy thermal photons that cannot be absorbed by the semiconductor. (a) Use a spectrally selective coating that will ideally emit high-energy photons or, (b) exploit the semiconductor band-edge itself as the spectral filter. The presence of a rear mirror ensures that any unabsorbed photons are reflected back to the emitter and are re-thermalized.

Serendipitously, such a rear mirror could also reflect below-bandgap photons (Fig. 1(b)). Unprecedented system efficiency can be achieved by reflecting low-energy photons back to reheat the thermal source while utilizing the high-energy photons for photovoltaic electricity. In effect, the semiconductor band-edge itself provides spectral selectivity, without the need for a spectrally-selective thermal emitter. This idea, first patented in 1967[30], relies on the re-use of low-energy photons[31], thus wasting no energy. We will call this process "Regenerative thermophotovoltaics".

Here, we present experimental results on a thermophotovoltaic cell with 29.1%±0.5% power conversion efficiency at an emitter temperature of 1207°C. This is a new record for thermo-photovoltaic efficiency. Our cells have an average reflectivity of 94.6% for below-bandgap photons, which is the key to recycling sub-bandgap photons. We predict that further improvements in reflectivity, series resistance, material quality, and the radiation chamber geometry will push system efficiency to >50%. Such a high-efficiency thermophotovoltaic system can have a significant impact as a power source for hybrid cars[32], unmanned vehicles[33], deep-space probes[34,35,36], energy storage[37,38] as well as enable efficient cogeneration systems[39,40,41] for heat and electricity.

The Regenerative Thermophotovoltaic System

In an ideal thermophotovoltaic system employing photon re-use (Fig. 2(a)), a hot emitter is surrounded by photovoltaic cells lining the walls of the chamber, collecting light from the emitter. For efficient recovery of unused photons, the photovoltaic cells are backed by highly reflective rear mirrors. Such mirrors are needed in any case to provide the voltage boost associated with luminescence extraction. As shown in Fig. 2(b), the below-bandgap recycled component of the radiated spectrum re-thermalizes within the emitter after being reflected from the photovoltaic cell.

Photon re-use in this chamber — enabled by high mirror reflectivity — results in high system efficiency. The system power conversion efficiency, η, is defined[42,43] as the electrical power generated by the photovoltaic cell, divided by the total thermal radiation power absorbed:

$$\eta = \frac{P_{\text{electrical}}}{P_{\text{incident}} - P_{\text{reflected}}} = \frac{P_{\text{electrical}}}{P_{\text{absorbed}}}, \quad \text{(1a)}$$

where P_{incident} is the incident power on the photovoltaic cell, and $P_{\text{reflected}}$ is the power

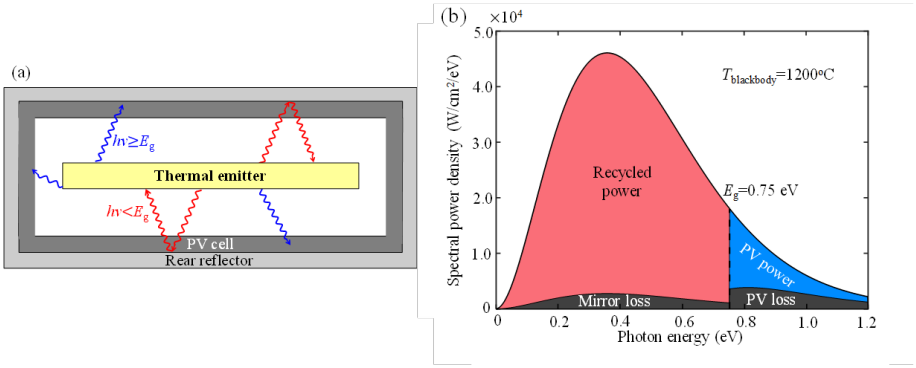

Figure 2: An ideal regenerative thermophotovoltaic system formed by a thermal radiation chamber, and power conversion inside the chamber. (a) High-energy (blue) photons from the emitter are converted to carriers in the photovoltaic cell, while low-energy (red) photons are reflected back to the emitter and re-thermalized. (b) A highly reflective rear mirror is essential since a photon will need to be reflected many times before emerging in the high energy tail of the Planck spectrum, for absorption in the semiconductor. Other losses in the photovoltaic cell arise due to poor material quality, as well as thermalization of high energy carriers.

reflected from the cell. Eq. (1a) is analogous to the efficiency definition of a solar cell, except that it accounts for the fact that reflected radiation is not lost but is re-thermalized at the thermal source. $P_{\text{reflected}}$ is taken from the measured reflectivity spectrum of the photovoltaic cell, while P_{incident} is obtained from an accurate calibration of emitter temperature.

Alternately:

$$\eta = \frac{P_{\text{electrical}}}{P_{\text{absorbed}}} = \frac{P_{\text{electrical}}}{P_{\text{electrical}}+Q_{\text{waste}}},$$

(1b)

which is the conventional definition of heat engine efficiency, where Q_{waste} is the waste heat.

Eq. (1a) and Eq. (1b) assume that the internal surfaces of the radiation chamber are completely covered by photovoltaic cells as shown in Fig. 2(a). To the extent that the internal walls are not fully covered by photovoltaic cells, the remaining area of bare walls needs excellent reflectivity to produce a good net "effective reflectivity" that controls the system efficiency.

The incident power $P_{\text{incident}}(T_s)$ at an emitter temperature T_s can be defined as the incident black body radiation flux $b_s(E, T_s)$ corrected by the spectral emissivity $\varepsilon(E)$ of the emitter (~0.91 for graphite[44]), integrated over energy and area:

$$P_{\text{incident}}(T_s) = A \int_0^\infty \varepsilon(E)\, b_s(E,T_s) \cdot E\, dE,$$

(2)

where E is the photon energy and A is the surface area of the photovoltaic cell. The cell absorptivity spectrum $a(E)$, used to determine P_{absorbed} which is the denominator in efficiency expression (Eq. 1(a) and 1(b)), can be directly known by

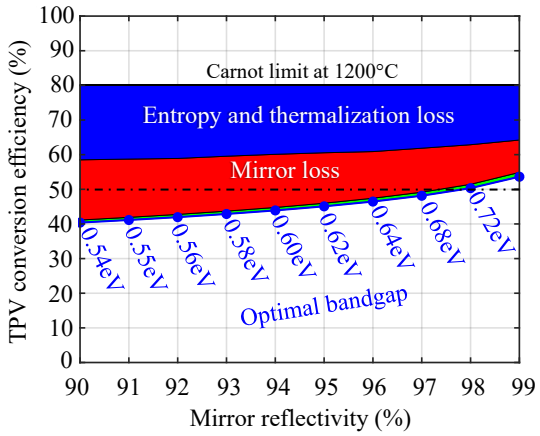

Figure 3: Projected thermophotovoltaic system conversion efficiency versus effective mirror reflectivity. As reflectivity rises, the optimum bandgap rises. In absence of a rear mirror, only 8.5% efficiency is possible. For this calculation, internal luminescence efficiency was assumed to be 98%, along with zero series resistance and unity emissivity.

measuring the cell reflectivity $R(E)$, since $a(E) = 1\text{-}R(E)$.

We can estimate the realistic thermophotovoltaic efficiency based on the quality of the existing III-V materials that contributed to the current record-holding solar

cells. The projected thermophotovoltaic efficiency is shown in Fig. 3, which represents a realistic efficiency projection rather than ideal Shockley-Queisser[45] performance. The optimum bandgap differs slightly for different rear reflectivities, to minimize thermalization loss of high-energy photons. This leads to an increase of the photovoltaic loss in the high-energy tail of Fig. 2(b). For an optimum bandgap, thermophotovoltaic efficiency can reach as high as >50%. If no rear mirrors are used, even with an ideal single-junction photovoltaic cell, only 8.5% efficiency is possible at 1200°C. For these calculations, we parameterized the material quality by internal luminescence efficiency η_{int} —the probability that carriers undergo radiative recombination— with a value η_{int}=98%.

Since the simple addition of a rear reflector can offer such high efficiencies, it is tempting to consider the possibility of combining the rear reflector photovoltaic cells, with a spectrally tuned emitter. For a spectrally tuned emitter with sub-bandgap reflectivity r ($\equiv 1-\varepsilon$), and a photovoltaic cell reflectivity R, the total loss due to parasitic absorption is dependent on both of these reflectivities, as obtained through geometric summation of multiple reflections between the emitter and the photovoltaic cell:

$$a_{\text{parasitic}} = \frac{(1-r)(1-R)}{1-rR}. \quad (3)$$

In this expression, either R or r will be close to unity.

With $R \sim 1$, the denominator of Eq. (3) becomes $1-r$, leaving the total parasitic absorptivity by the quality of the rear mirror. On the other hand, if $r \sim 1$, then the total parasitic absorptivity $a_{\text{parasitic}} \sim 1-r$. Hence in the presence of excellent emissivity control, the performance is almost entirely dominated by the high thermal emitter spectral reflectivity r. Whichever of R or r is closer to unity will dominate, and further improvements in the other, non-dominant reflectivity, r or R will not contribute significantly. Thus, there is little further benefit in combining Fig. 1(a) and Fig. 1(b).

Thermophotovoltaic Cell Modelling

In this section, we describe the procedures for modeling thermophotovoltaic cells, in the regenerative approach.

The current density J in the photovoltaic cell can be described as $J(T_s, V) = J_L(T_s) - J_{diode}(V)$, where J_L is photo-generated current density and J_{diode} is the current arising from carrier removal, as a consequence of the bias applied to the diode. This diode current has three main components; (a) carriers that recombine radiatively and produce photons that escape out of the device (J_{esc}), (b) carriers that produce photons that are lost by parasitic absorption in the mirror (J_{mirror}) and, (3) carriers that are lost

due to non-radiative SRH or Auger recombination within the device (J_{nrad}). Hence, we can write J as:

$$J(T_s, V) = J_L(T_s) - J_{esc}(V) - J_{mirror}(V) - J_{nrad}(V) \quad (4)$$

We can calculate $J_L(T_s)$ for an arbitrary emitter temperature T_s from Eq. (5), where $a(E)$ is the absorptivity spectrum and IQE(E) is the internal quantum efficiency—a fraction of the generated carriers that is extracted by the electrical contacts—of the cell. For a cell with planar geometry, we can express $a(E)$ with Eq. (6), where T_{front} is the transmissivity of the front surface, and $R_{rear}(E)$ is the reflectivity of the rear mirror. T_{front} was taken to be 65.5%, obtained from an above-bandgap spectral average of the measured reflectivity spectrum, and IQE was taken to be 98%, accounting for a small loss due to non-unity carrier collection efficiency. The absorption co-efficient $\alpha(E)$ is taken as the average of that of GaAs and InAs, weighted by material composition, similar to Ganapati et. al. [46].

$$J_L(T_s) = q \int_0^\infty a(E) b_s(T_s, E) \mathrm{IQE}(E)\, dE \quad (5)$$

$$a(E) = T_{front} \frac{(1-\exp(-\alpha(E)L))}{1-(1-T_{front})R_{rear}(E)\exp(-2\alpha(E)L)} (1 + R_{rear}(E)\exp(-\alpha(E)L)) \quad (6)$$

An internal luminescent current exists within the device (J_{rad}) under an applied bias. The portion of this internal current that escapes through the front, $J_{esc}(V)$can be expressed is $P_{esc} \cdot J_{rad}(V)$, where P_{esc} as the escape probability of a photon that is inside the device. We can express P_{esc} as in Eq. (7), which has been derived by Rau et. al.[47]. The temperature of the cell is denoted by T_c. For this calculation, we used the refractive index n_r=3.5. We can calculate $J_{rad}(V)$ from the modified Shockley-Van-Roosebroeck relationship, as in Eq. (8)[48].

$$P_{esc} = \frac{\int_0^\infty a(E) b_s(T_c,E)\, dE}{\int_0^\infty 4n_r^2 L \alpha(E) b_s(T_c,E) dE} \quad (7)$$

$$J_{rad}(V) = q \frac{2\pi L}{c^2 h^3} \int_0^\infty 4n_r^2 E^2 \alpha(E) \exp\left(\frac{qV-E}{K_b T_c}\right) dE \quad (8)$$

A portion of the radiative recombination current is lost by mirror absorption, rather than extracted through the front surface. The mirror loss can be expressed as $P_{mirror}J_{rad}$(V), where P_{mirror} is the probability that an internally emitted photon is absorbed by the mirror. This probability is given by Eq. (9), where $a_{rear}(E, \Theta)$ is the absorptivity of the mirror for photons internally emitted inside the semiconductor. The expression for a_{rear} can be found by equating the rate of absorption of luminescent photons by the rear to the mirror's rate of thermal radiation. An expression for $a_{rear}(E, \Theta)$ in a planar structure such as ours has been derived in

Ganapati et. al.[49], and is given by Eq. (10), where $\Theta_c = \sin^{-1}(1/n_r)$ is the critical angle of the front air-semiconductor interface. In Eq. (9), we have a factor of n_r^2 which is absent in Eq. (6). This is because the mirror radiates into the semiconductor, where the density of electromagnetic modes is greater by a factor of n_r^2 relative to air.

$$P_{\text{mirror}} = \frac{\int_0^\infty n_r^2 a_{\text{rear}}(E,\Theta)(E) b_s(E,T_c) dE}{\int_0^\infty 4 n_r^2 L \alpha(E) b_s(E,T_c) dE} \quad (9)$$

$$a_{\text{rear}}(E,\Theta) = (1 - R_{\text{rear}}) \times \begin{cases} 1 - \exp\left(-\frac{\alpha(E)L}{\cos\Theta}\right), & \text{if } \Theta < \Theta_c \\ \frac{1-\exp\left(-\frac{2\alpha(E)L}{\cos\Theta}\right)}{1-R(E)\exp\left(-\frac{2\alpha(E)L}{\cos\Theta}\right)}, & \text{if } \Theta \geq \Theta_c \end{cases} \quad (10)$$

The remaining component $J_{\text{nrad}}(V)$, can be estimated from the internal luminescence efficiency $\eta_{\text{int}}(V)$, expressed as:

$$\eta_{\text{int}}(V) = \frac{J_{\text{rad}}(V)}{J_{\text{rad}}(V)+J_{\text{nrad}}(V)}. \quad (11)$$

Re-arranging terms, we get

$$J_{\text{nrad}}(V) = \left(\frac{1}{\eta_{\text{int}}(V)} - 1\right) J_{\text{rad}}(V). \quad (12)$$

Knowing the *J-V* under any illumination, we can then estimate the $\eta_{\text{int}}(V)$ using Eq. (3)-(11), and vice versa.

Finally, we include the effects of the series resistance R_s and the shunt resistance R_{sh} by using the modified current equation, Eq. (13). We can account for the effect of series resistance by replacing the terminal voltage V in Eq. (4)-(12) with $V+J\cdot R_s\cdot A$, which is the quasi-Fermi level splitting inside the InGaAs layer. We can estimate the series resistance R_s from the slope of the measured I-V curve at open-circuit voltage, which gives R_s= 0.43Ω. Fitting the measured dark *J-V* curve to Eq. (13), this leads to an average η_{int}= 82% and shunt resistance R_{sh}= 852Ω. Details of these measurements will be elaborated on in the next section.

We note that near the operating voltage of the cell, the effect of R_{sh} is minimal, and hence the deviation of our photovoltaic cell performance from ideal is determined by the values of R_s, $R(E)$, and $\eta_{\text{int}}(V)$.

$$J(T_s, V + JR_sA) = J_L(T_s) - J_{\text{esc}}(V + JR_sA) - J_{\text{mirror}}(V + JR_sA) - J_{\text{nrad}}(V + JR_sA) - \frac{V+JR_sA}{R_{sh}A} \quad (13)$$

Knowing the value of $\eta_{int}(V)$ allows us to calculate the SRH lifetime, τ_{SRH} for this device, using Eq. (13), where n and p are the electron and hole concentration and n_i as the intrinsic carrier density. We used the Auger coefficients C_n and C_p to be $8.1\times10^{-29}cm^6s^{-1}$ from the experimental data of Ahrenkiel et. al.[50]. To calculate the carrier densities, we used the reported values of the electronic parameters of InGaAs[51].

$$J_{nrad} = L\left[\frac{np-n_i^2}{\tau_{SRH}(n+p+2n_i)} + (C_n n + C_p p)(np - n_i^2)\right] \quad (141)$$

Fitting the measured value of η_{int} to this expression yields τ_{SRH}= 60 ns. With improved materials processing, there is potential to increase this lifetime by more than two orders of magnitude [50], which in turn would increase the value of η_{int}= 98%.

References

[1] R. E. Nelson, "A brief history of thermophotovoltaic development," *Semicond. Sci. Technol.*, vol. 18, no. 5, p. S141, 2003.

[2] H. Daneshvar, R. Prinja, and N. P. Kherani, "Thermophotovoltaics: fundamentals, challenges, and prospects," *Appl. Energ.*, vol. 159, pp. 560—575, December 2015.

[3] T. J. Coutts, "A review of progress in thermophotovoltaic generation of electricity," *Renew. Sust. Energy Rev.*, vol. 3, no. 2-3, pp. 77—184, September 1999.

[4] B. Bitner, W. Durisch, and R. Holzner, "Thermophotovoltaics on the move to applications," *Appl. Energ.*, vol. 105, pp. 430—438, May 2013.

[5] A. Luque, "Solar thermophiotovoltaics: Combining solar thermal and photovoltaics," *AIP Conference Proceedings*, vol. 890, no. 1, pp. 3—16, 2007.

[6] C. Ferrari, F. Melino, M. Pinelli, P. R> Spina, and M. Venturini, "Overview and status of thermophotovoltaic systems," *Energy Procedia*, vol. 45, pp. 160—169, 2014.

[7] P. Aigrain, "Thermophotovoltaic conversion of radiant energy," Unpublished lecture series at MIT, 1956.

[8] T. D. Rahmlow Jr, D. M. DePy, P. M. Fourspring, H. Ehsani, J. E. Lazo-Wasem, and E. J. Gratrix, "Development of front surface, spectral control filters with greater temperature stability for thermophotovoltaic energy conversion," *AIP Conference Proceedings*, vol. 890, no. 1, pp. 59—67, 2007.

[9] Z. Jurado, J. Kou. S. M. Kamali, A. Faraon, and A. J. Minnich, "Wavelength-selective thermal extraction for higher efficiency and power density thermophotovoltaics," *J. Appl. Phys*., vol. 124, no. 18, pp. 183105, 2018.

[10] P. Wurfel, and W. Ruppel, "Upper limit of thermophotovoltaic solar-energy conversion," *IEEE Trans. Electron. Devices*, vol. 27, no. 4, pp. 745—750, April 1980.
[11] J. K. Tong, W. Hsu, Y. Huang, S. V. Boriskina, and G. Chen, "Thin-film thermal well emitters and absorber for high-efficiency thermophotovoltaics," *Sci. Rep.*, vol. 5, pp. 10661—10673, June 2015.
[12] J. M. Gee, J. B. Moreno, Shawn-Yu Lin, and J. G. Fleming, "Selective emitters using photonic crystals for thermophotovoltaic energy conversion," *Conference Record of the Twenty-Ninth IEEE Photovoltaic Specialists Conference*, pp. 896–899, 2002.
[13] W.R. Chan, V. Stelmakh, M. Ghebrebrhan, M. Soljačić, J. D. Joannopoulos, and I. Celanović, "Enabling efficient heat-to-electricity generation at mesoscale," *Energy Envrion. Sci.*, vol. 10, no. 6, p. 1367, June 2017.
[14] P. Bermel et. al., "Design and global optimization of high-efficiency thermophotovoltaic systems," *Opt. Exp.*, vol. 18, no. 53, pp. A314—A334, August 2010.
[15] E. Rephaeli, and S. Fan, "Absorber and emitter for solar thermophotovoltaic systems to achieve efficiency exceeding the Shockley-Queisser limit," *Opt. Exp.*, vol. 17, no. 17, pp. 15145—15159, August 2009.
[16] P. V. Braun et. al., "Three-dimensional self-assembled photonic crystals with high temperature stability for thermal emission modification," *Nat. Com.*, vol. 4, October 2010.
[17] A. Lenert, D. M. Bierman, Y. Nam, W. Chan, I. Celanović, Marin Soljačić, and E. W. Wang, "A nanophotonic solar thermophotovoltaic device," *Nat. Nano.*, vol. 9, pp. 126—130, February 2014.
[18] A. S. Vlasov, V. P. Khvostikov, O. A. Khvostikova, P. Y. Gazaryan, S. V. Sorokina, and V. M. Andreev, "TPV systems with solar powered tungsten emitters," *AIP Conference Proceedings*, vol. 890, no. 1, pp. 327—334, 2007.
[19] D. N. Woolf et al., "High-efficiency thermophotovoltaic energy conversion enabled by a metamaterial selective emitter," *Optica*, vol. 5, no. 2, pp. 213–218, Feb. 2018.
[20] C. Wu, B. Neuner III, J. John, A. Milder, B. Zollars, S. Savoy, and G. Shvets, "Metamaterial-based integrated plasmonic absorber/emitter for solar thermo-photovoltaic systems," *J. Opt.*, vol. 14, no. 2, January 2012.
[21] S. Molesky, C. J. Dewalt, and Z. Jacob, "High temperature epsilon-near-zero and epsilon-near-pole metamaterial emitters for thermophotovoltaics," *Opt. Exp.*, vol. 21, no. S1, pp. A96—A110, 2013.
[22] C. Chang, W. J. M. Kort-Kamp, J. Nogan. T. S. Luk, A. K. Azad, A. J. Taylor, D. A. R. Dalvit, M. Sykora, and H. Chen, "High-temperature refractory

metasurfaces for solar thermophotovoltaic energy harvesting," *Nano Lett.*, vol. 18, no. 12, pp. 7665—7673, November 2018.
[23] K. Kevin, "GRI research on thermophotovoltaics," *AIP Conference Proceedings*, vol. 321, no. 1, pp. 54—63, 1995.
[24] R. A. Lowe, D. L. Chubb, and B. S. Good, "Radiative performance of rare earth garnet thin film selective emitters," *AIP Conference Proceedings*, vol. 321, no. 1, pp. 291—297, 1995.
[25] This is sometimes attributed to Photon Recycling, but it is more accurate to cite Luminescence Extraction as the voltage boost mechanism. E. Yablonovitch, "Photon recycling versus luminescence extraction for record photovoltaic efficiency", in "Roadmap on optical energy conversion" ed. by S.V. Boriskina, M.A. Green, K. Catchpole, Kylie; et al., *J. of Optics*, vol. 18, no. 7, July 2016.
[26] B. M. Kayes et. al., "27.6% conversion efficiency, a new record for single-junction solar cells under 1 sun illumination," *2011 37th IEEE Photovoltaic Specialists Conference, pp. 000004—000008, 2011.*
[27] O. D. Miller, E. Yablonovitch, and S. R. Kurtz, "Strong internal and external luminescence as solar cells approach the Shockley-Queisser limit," *IEEE J. Photovolt.*, vol. 2, no. 3, pp. 303–311, Jul. 2012.
[28] M. A. Steiner, J. F. Geisz, I. García, D. J. Friedman, A. Duda, and S. R. Kurtz, "Optical enhancement of the open-circuit voltage in high quality GaAs solar cells," *J. Appl. Phys.*, vol. 113, no. 12, p. 123109, Mar. 2013.
[29] V. Ganapati, M. A. Steiner, and E. Yablonovitch, "The voltage boost enabled by luminescence extraction in solar cells," *IEEE J. Photovolt.*, vol. 6, no. 4, pp. 801–809, Jul. 2016.
[30] J. J. Werth, "Thermo-photovoltaic converter with radiant energy reflective means," Jul. 1967.
[31] R. M. Swanson, "Silicon photovoltaic cells in thermophotovoltaic energy conversion," in *1978 International Electron Devices Meeting*, 1978, vol. 24, pp. 70–73.
[32] O. Morrison, S. Michael, W. Edward, and C. William, "Use of a thermophotovoltaic generator in a hybrid electric vehicle," *AIP Conference Proceedings*, vol. 460, no. 1, pp. 488—496, 1999.
[33] G. A. Holmquist, "TPV power source development for an unmanned undersea vehicle*," AIP Conference Proceedings*, vol. 321, no. 1, pp. 308—314, 1995.
[34] D. Wilt, D. Chubb, D. Wolford, P. Magari, and C. Crowley, "Thermophotovoltaics for space power applications," *AIP Conference Proceedings*, vol. 890, no. 1, pp. 335—345, 2007.
[35] A. Schock, and V. Kumar, "Radioisotope thermophotovoltaic system design and its application to an illustrative space mission," *AIP Conference Proceedings*, vol. 321, no. 1, pp. 139—152, 1995.

[36] V. L. Teofilo, P. Choong, J. Chang, Y. L. Tseng, and S. Ermer, "Thermophotovoltaic energy conversion for space," *J. Phys. Chem. C.*, vol. 118, no. 21, pp. 7841—7845, 2008.
[37] A. Datas, D. Chubb, A Veeraragavan, "Steady state analysis of a storage integrated solar thermophotovoltaic system," *Solar Energy*, vol. 96, pp. 33—45, Aug 2013.
[38] C. Amy, H. R. Seyf, M. A. Steiner, D. J. Friedman, and A. Henry, "Thermal energy grid storage using multi-junction photovoltaics," *Energy Environ. Sci.*, vol. 12, pp. 334—343, 2019.
[39] T. A. Butcher, J. S. Hammonds, E. Horne, B. Kamath, J. Carpenter, and D. R. Woods, "Heat transfer and thermophotovoltaic power generation in oil-fired heating systems," *App. Energ.*, vol. 88, no. 5, pp. 1543—1548, May 2011.
[40] L. M. Fraas, "Economic potential for thermophotovoltaic electric power generation in the steel industry", *2014 IEEE 40th Photovoltaic Specialist Conference (PVSC), pp. 0766—0770, 2014.*
[41] M. Bianchi, C. Ferrari, F. Melino, and A. Peretto, "Feasibility study of a thermos-photo-voltaic system for CHP application in residential buildings," *Appl. Energ.*, vol. 97, pp. 704—713, September 2012.
[42] B. Wernsman et al., "Greater than 20% radiant heat conversion efficiency of a thermophotovoltaic radiator/module system using reflective spectral control," *IEEE Trans. Electron Devices*, vol. 51, no. 3, pp. 512–515, Mar. 2004.
[43] G. W. Charache et. al., "Measurement of conversion efficiency of thermophotovoltaic devices," *AIP Conference Proceedings*, vol. 358, no. 1, pp. 351—360, 1996.
[44] G. Neuer, "Spectral and total emissivity measurements of highly emitting materials," *Int. J. Thermophys.*, vol. 16, no. 1, pp. 257–265, Jan. 1995.
[45] W. Shockley and H. J. Queisser, "Detalied balance limit of efficiency of *p-n* junction solar cells," *J. Appl. Phys.*, vol. 32, no. 3, pp. 510–519, Mar. 1961.
[46] V. Ganapati, T. Patrick Xiao, and E. Yablonovitch, "Ultra-efficient thermophotovoltaics exploiting spectral Filtering by the Photovoltaic Band-Edge," *ArXiv161103544 Phys.*, Nov. 2016.
[47] U. Rau, U. W. Paetzold, and T. Kirchartz, "Thermodynamics of light management in photovoltaic devices," *Phys. Rev. B*, vol. 90, no. 3, p. 035211, Jul. 2014.
[48] W. van Roosbroeck and W. Shockley, "Photon-Radiative Recombination of Electrons and Holes in Germanium," *Phys. Rev.*, vol. 94, no. 6, pp. 1558–1560, Jun. 1954.
[49] V. Ganapati, M. A. Steiner, and E. Yablonovitch, "The Voltage Boost Enabled by Luminescence Extraction in Solar Cells," *IEEE J. Photovolt.*, vol. 6, no. 4, pp. 801–809, Jul. 2016.

[50] R. K. Ahrenkiel, R. Ellingson, S. Johnston, and M. Wanlass, "Recombination lifetime of In0.53Ga0.47As as a function of doping density," *Appl. Phys. Lett.*, vol. 72, no. 26, pp. 3470–3472, Jun. 1998.
[51] "Recombination Parameter of Gallium Indium Arsenide (GaInAs)." [Online]. Available: http://www.ioffe.ru/SVA/NSM/Semicond/GaInAs/recombination.html#Recombination. [Accessed: 16-Apr-2018].

2. Regenerative Thermophotovoltaics: Experiment

In this section, we discuss our efforts to experimentally measure thermophotovoltaic power conversion efficiency.

Photovoltaic cell design and fabrication

The devices were fabricated at National Renewable Energy Laboratory. We use a thin-film $In_{0.55}Ga_{0.45}As$ photovoltaic cell with a bandgap of 0.75eV (Fig. 1). InGaAs, like all III-V semiconductors, can have an excellent radiative recombination coefficient[1]. The device is a heterojunction structure where the active material is sandwiched between a hole selective p-InP layer, and an electron selective n-InP layer. These two heterojunction layers are ohmically contacted by thin, heavily-doped, front n-InGaAs and rear p-InGaAsP layers, which are covered by thin-film Au electrodes. The Au electrodes are then connected to the external circuit using aluminum wire bonds. We note that while the front electrode grid might induce shadowing losses in a typical photovoltaic system, in our thermophotovoltaic system those photons are reflected back into the emitter and recovered. Indeed, the reflectivity of the Au/Air interface is 98%, and therefore parasitic absorption by the front electrode is negligible. Moreover, the InGaAsP and InP heterojunction layers in the device have a higher bandgap (1eV and 1.34eV respectively) than the active layer (0.75eV), to ensure that parasitic absorption within these layers is also minimized.

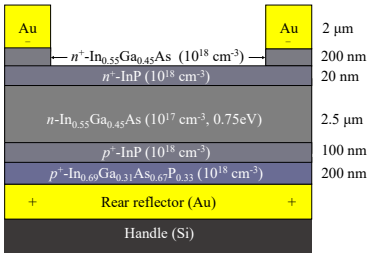

Fig. 1: The InGaAs active layer has a bandgap of 0.75eV. The rear Au layer acts as the reflective mirror. Electrons are collected by the front electrode grid, while holes are collected by the rear Au layer.

These layers are grown by atmospheric pressure metalorganic vapor phase epitaxy on an InP substrate. The growth is inverted, with the top layer grown first, and the device is re-oriented during post-growth processing. After the deposition of the gold film—which is used both as the mirror and the positive electrode—the layer stacks are then attached to a silicon handle using a thermally conductive epoxy. The InP substrate is then totally etched away.

Experimental Chamber

The experimental chamber used for the thermophotovoltaic measurements is shown in Fig. 2. The thermal emitter is a graphite ribbon. Current is injected into the ribbon through its short edges to raise the temperature by Joule heating. Beneath the ribbon,

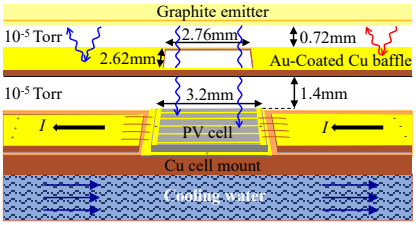

Fig. 2 Experimental setup for the thermophotovoltaic efficiency calibration. The graphite emitter is heated by Joule heating. The cell sits under a baffle, to minimize any stray photons reaching the cell. The wire bonds are made separately, to the top and bottom electrodes, for electrons and holes respectively. The cell is cooled to a standard temperature, 25°C. Current (I) and voltage are measured by wire-bonding the cell to electrical pads.

the photovoltaic cell is placed on a copper mount using thermally conductive epoxy. The photovoltaic cell is placed under a copper baffle that provides an aperture for defining the incident radiation pattern. The inner walls of the baffle are coated with a highly absorptive black coating, to eliminate stray photons between the baffle and the photovoltaic cell. This replicates the situation in a thermophotovoltaic system with an emitter fully surrounded by photovoltaic cells, where these stray reflected photons would be re-captured by the heat source. The entire system is placed inside a vacuum chamber with a pressure of 10^{-5} Torr. The vacuum minimizes any parasitic heat conduction from the emitter to the photovoltaic cell.

Efficiency Calibration

We describe two different efficiency calibration procedures for regenerative thermophotovoltaics. The first procedure is based on a measurement of external quantum efficiency and thermophotovoltaic cell absorptivity and offers better accuracy. The second approach is based on the measurement of cell absorptivity alone, with an estimation of the internal quantum efficiency of the cell. This approach, has the advantage of being simpler, however does not offer the same accuracy as the first approach.

External Quantum Efficiency-based Approach

Under the regenerative principle, the reflected photon flux from the photovoltaic cell reheats the thermal emitter and does not count against the measured efficiency. Hence, the measurement of the power conversion efficiency $\eta = \frac{P_{\text{electrical}}}{P_{\text{incident}} - P_{\text{reflected}}} = \frac{P_{\text{electrical}}}{P_{\text{absorbed}}}$ of a thermophotovoltaic device requires measurement of the total generated power ($P_{\text{electrical}}$), the incident power P_{incident}, as well as the reflected thermal power ($P_{\text{reflected}}$) by the device.

In an absolute calibration, the numerator is the electrical power which is very easy to measure. But the power absorbed is difficult to know, since it depends on multiple parameters.

To measure the incident photon flux we need to know (*i*) the emissivity of the emitter, (*ii*) the geometrical view factor F_{eff}, the fractional solid angle subtended by the emitter as viewed from the photovoltaic cell, as well as the multiple reflections between the photovoltaic cell, emitter and the baffle used in our chamber, and (*iii*) the temperature of the emitter.

We establish methods to measure each of these parameters.

(*i*) The emissivity ε of graphite was measured, obtaining a value of $\varepsilon \sim 0.91$, similar to other literature reports[5].

(*ii*) The geometrical view factor determines the short-circuit current from a black body. We calibrate the emitter temperature at 1085°C by slowly increasing the supplied electrical power until a copper bead that was previously placed on top of the emitter reaches its solid-to-liquid transition. Thus by measuring the short-circuit current at exactly 1085°C, we obtain the geometrical view factor. The relationship between the short-circuit current, view factor and Planck spectrum can be expressed with the following equation:

$$I_{SC}(T_s) = qAF_{\text{eff}} \int_0^\infty \varepsilon_{\text{eff}}((E)\ \text{EQE}(E)\ \ b_s(E,T_s)dE. \qquad (1)$$

For calibration of F_{eff}, we use the black body Planck spectrum $b_s(E, T_s)$ at a calibrated emitter temperature T_s=1085°C, EQE(E) is the measured external quantum efficiency, and $\varepsilon_{\text{eff}}(E)$ is the effectivity emissivity[1] spectrum. From this, we extract a view factor F_{eff} =0.31. We have the spectrum as $b_s(E, T_s)dE = \frac{2\pi E^3}{c^2\hbar^3(exp(\frac{E}{k_B T})-1)}\,dE$.

(*iii*) Since the above procedure calibrates the geometrical view factor, which is temperature-independent, we can then solve Eq. (1) to find the emitter temperature when $T_s \neq 1085$°C.

Since we know the effective emissivity, geometrical view factor, and emitter temperature, we can accurately measure the incident flux $P_{\text{incident}}(T_s) = AF_{\text{eff}} \int_0^\infty \varepsilon_{\text{eff}}(E)\, b_s(E,T_s) \cdot EdE$.

We need to convert the incident spectrum to an absorbed spectrum since any unabsorbed portion of the incident spectrum will be reflected back to the thermal emitter. Finally, we measure the device's absorptivity spectrum as (1-reflectivity). The total absorbed power in the photovoltaic device is then:

$$P_{\text{absorbed}}(T_s) = P_{\text{incident}} - P_{\text{reflected}} = AF_{\text{eff}} \int_0^\infty \varepsilon_{\text{eff}}(E) \left(1 - R(E)\right) b_s(E,T_s) \cdot EdE \qquad (2)$$

With (*i*) emissivity calibration, (*ii*) view factor calibration, and (*iii*) temperature calibration, we can now accurately characterize the device thermophotovoltaic efficiency.

Internal Quantum Efficiency-based Approach

The thermophotovoltaic efficiency is the ratio of the electrical power extracted to the power absorbed by the cell. The measurement of the electrical power extracted from the thermophotovoltaic cell, $P_{\text{electrical}}$, is routine. We make wire bonds to the cell electrodes, as shown in Fig. 2, and measure the current-voltage response. Measurement of the absorbed power depends on the measurement of the cell reflectivity and the incident thermal radiation. Incident thermal radiation on the cell depends on three factors; (i) temperature of the emitter (T_s), (ii) emissivity ε of the graphite emitter, and (iii) the geometric view factor F, which is the solid angle subtended by the emitter as seen from the thermophotovoltaic cell, controlled by a geometric baffle. Together with the surface area A_{cell} of the thermophotovoltaic cell, the incident power is $P_{\text{incident}}(E, T_s)=A_{\text{cell}}\varepsilon F_{\text{eff}} b_s(E, T_s)dE$. We are introducing an effective view factor F_{eff} to take into account the multiple photon bounces. The effective view factor is also dependent on the graphite emissivity owing to multiple photon reflections between the graphite emitter and the thermophotovoltaic cell. In our method of calibration detailed geometric analysis is unnecessary since $\varepsilon F_{\text{eff}}$ can be obtained directly from the observed short-circuit current.

Using the expression of P_{incident}, we can measure the power absorbed P_{absorbed} by the thermophotovoltaic cell as:

$$P_{absorbed}(T_s) = A_{cell}\varepsilon F_{eff}\int_0^\infty \{1 - R(E)\}b_s(E, T_s)dE \qquad (3)$$

Note that we are ignoring the photon energy dependence of the emissivity, and its temperature dependence, based on the experimental evidence that such dependency is very weak[5]. We now describe the procedure to calibrate the emitter temperature T_s, and the power absorbed $P_{\text{absorbed}}(T_s)$ by the thermophotovoltaic cell. These can be calibrated directly from the short-circuit current of the thermophotovoltaic cell.

Under illumination from a thermal emitter at temperature T_s, we can express the short-circuit current as:

$$J_{sc}(T_s) = qA_{cell}\varepsilon F_{eff}\int_0^\infty EQE(E)\cdot\frac{b_s(E, T_s)}{E}dE \qquad (4)$$

We can isolate $\varepsilon F_{\text{eff}}$ on the left as:

$$\varepsilon F_{eff} = \frac{J_{sc}(T_s)}{qA_{cell}\int_0^\infty EQE(E)\cdot\frac{b_s(E, T_s)}{E}dE} \qquad (4')$$

where q is the electron charge and the external quantum efficiency, and EQE is the probability that a photon incident on the photovoltaic cell generates an electron-hole pair and is electrically extracted. We can write EQE as $C\times(1\text{-}R)$, where C is the internal quantum efficiency of the thermophotovoltaic cell. C is zero below the bandgap. We can replace EQE with $C\times(1\text{-}R)$ and change from 0 to E_g the lower limit of the denominator integral :

$$\varepsilon F_{eff} = \frac{J_{sc}(T_s)}{qA_{cell}C\int_{E_g}^{\infty}\{1-R(E)\}\cdot\frac{b_s(E,\,T_s)}{E}dE} \qquad (5)$$

where we have pulled C out of the integral. We assume spectrally averaged C to be relatively constant.

We now discuss our procedure for measuring $R(E)$ and C to measure emitter temperature T_s, using Eq. (5). Once we know the reflectivity $R(E)$ and internal quantum efficiency C at emitter temperature T_s, the corresponding short-circuit current $J_{sc}(T_s)$ calibrates the emissivity-view factor product εF_{eff}.

We calibrate the emitter to a reference temperature T_s=1085°C by placing a copper particle on top of the graphite ribbon emitter and monitor its melting point by a change in color. We then measure the reference short-circuit current and the open-circuit voltage at T_s=1085°C. We can infer the average internal quantum efficiency C from the measured voltage at the reference temperature T_s=1085°C. Photon absorption primarily happens in the active layer. The generated electron-hole pairs are then efficiently transported to the electrical contacts. The internal quantum efficiency of the thermophotovoltaic cell is the product of the transport efficiency, and the optical absorption fraction inside the active layer. We can calculate the transport efficiency using the familiar base transport efficiency[2] expression T_r=[1-(L/L_D)^2], where L is the diffusing distance, and L_D is the diffusion length $\sqrt{(D\tau)}$.

We have done a careful calibration of the internal photo-luminescence efficiency in the presence of photon recycling, taking mirror reflectivity into account. As in many modern photovoltaic cells, the internal photoluminescence efficiencies in our thermophotovoltaic cells are quite high, ~85%. This is not as good as ~96% photo-luminescence efficiency of the record-breaking GaAs cells[3]. The luminescent photons are absorbed and re-emitted many times. Thus the actual radiative minority carrier lifetime is 1/(1-0.85)~6.7× longer than in the case of the lifetime in optically absorbing surroundings.

To determine the internal quantum efficiency C, we need the diffusion length $\sqrt{(D\,\tau)}$ which contains the carrier lifetime $\tau\equiv 1/(BN)$ where B is the bimolecular radiative recombination co-efficient, and N is the majority carrier doping. But then we need to multiply that lifetime by 6.7, for photon recycling. We used an active n-layer doping N=10^{17}cm^{-3}. The minority hole diffusion constant in the n-type InGaAs active layer is D=7.5 cm^{2}s^{-1}[4]. This value was measured in the lattice-scattering-dominated regime of mobility. Ahrenkiel et. al. reported a radiative recombination coefficient B = 1.43×10^{-10} cm^{3}s^{-1} **Error! Bookmark not defined.** for an air-$In_{0.53}Ga_{0.47}As$-InP structure. Therefore τ~70nsec. Accounting for photon recycling

by multiplying by 6.7, the radiative minority lifetime becomes τ~470nsec. The non-radiative in these high-quality materials is even longer τ~2μsec.
This gives us a minority carrier diffusion length = $\sqrt{D\tau}$~19μm.
The active layer thickness is 2.5μm. In our case, the diffusing distance L is half the active layer thickness, L=1.25μm for the following reason. The photon recycling events spread the minority carriers evenly throughout the active thickness, and so the average diffusing distance is halved. This produces a transport efficiency T_r=99.6%, which must be multiplied by the optical absorption fraction [1-exp{-2αL}]=99.3% for double-pass absorption with α=10^4/cm, near the band-edge. The product of T_r and the absorption fraction is C=98.9%, and we note $EQE \equiv C \times (1-R)$.
Alternately, we measure EQE from spectrally resolved short-circuit, as shown in Fig. 3(b). The internal quantum efficiency C=99.2% estimated from spectrally resolved short circuit current is a close match to the C=98.9% estimated from the diffusion length.
Eq. (5), combined with known graphite temperature, known short-circuit current, measured absorptivity {1-R}, and measured internal quantum efficiency calibrates the emissivity-view factor product εF_{eff}=0.32. For the given emissivity-solid angle product, only 32% of the potential short circuit current was collected.
We can then use this measured εF_{eff}, for calibration of emitter temperatures other than T_s=1085°C, by the changed short circuit current at each temperature. At each temperature T_s, we use the measured C and the spectrally resolved absorptivity {1-$R(E)$} to obtain the emitter temperature.
The emitter temperature T_s and the electrical power generated $P_{electrical}(T_s)$, are steps toward the thermophotovoltaic cell efficiency $\eta(T_s) \equiv P_{electrical}(T_s)/P_{absorbed}(T_s)$. We now describe the procedure for calibrating the denominator $P_{absorbed}(T_s)$.
We can explicitly determine $P_{absorbed}$ at emitter temperature T_s, by plugging Eq. (4') into Eq. (3) as follows:

$$P_{absorbed}(T_s) = \frac{J_{sc}(T_s) \int_0^\infty \{1-R(E)\} b_s(E,T_s) dE}{q \int_0^\infty EQE(E) \cdot \frac{b_s(E,\ T_s)}{E} dE} \qquad (6)$$

We can substitute EQE with $C \times (1-R)$ and change the lower limit on the denominator integral from 0 to E_g, similar to Eq. (5):

$$P_{absorbed}(T_s) = \frac{J_{sc}(T_s) \int_0^\infty \{1-R(E)\} b_s(E,T_s) dE}{q \int_{E_g}^\infty C\,\{1-R(E)\} \cdot \frac{b_s(E,\ T_s)}{E} dE}$$

$$= \frac{J_{sc}(T_s)}{q}\left[\left(\frac{1-R_{below}}{1-R_{above}}\right)\frac{1}{C}\frac{\int_0^{E_g} b_s(E,T_s)dE}{\int_{E_g}^{\infty}\frac{b_s(E,\,T_s)}{E}dE} + \frac{1}{C}\frac{\int_{E_g}^{\infty} b_s(E,T_s)dE}{\int_{E_g}^{\infty}\frac{b_s(E,\,T_s)}{E}dE}\right] \quad (7)$$

where, R_{below} and R_{above} are the spectral average reflectivities, below and above the band-edge photon energy, respectively. The reflectivities R_{below} and R_{above} averaged over round-trip oscillations, are taken as constant and removed from under the integrals. We have already measured the internal quantum efficiency C=98.9% in Eq. (7). There are three black-body integrals in Eq. (7) that are also exactly known since the temperature T_s is accurately calibrated. The power conversion efficiency is a ratio of useful electrical power to the total thermal power absorbed by the thermophotovoltaic cell.

Measurement of reflectivity and external quantum efficiency

We measure the reflectivity of our cells are measured using a Fourier transform infrared (FTIR) spectrometer. The result from one of the devices is shown in Fig. 3(a). The incident and reflected light pass through a microscope objective with a numerical aperture (NA)=0.65, which corresponds to an angular reflectivity averaged over an incidence angle range, of 0° to 36° from normal. The reflectivity

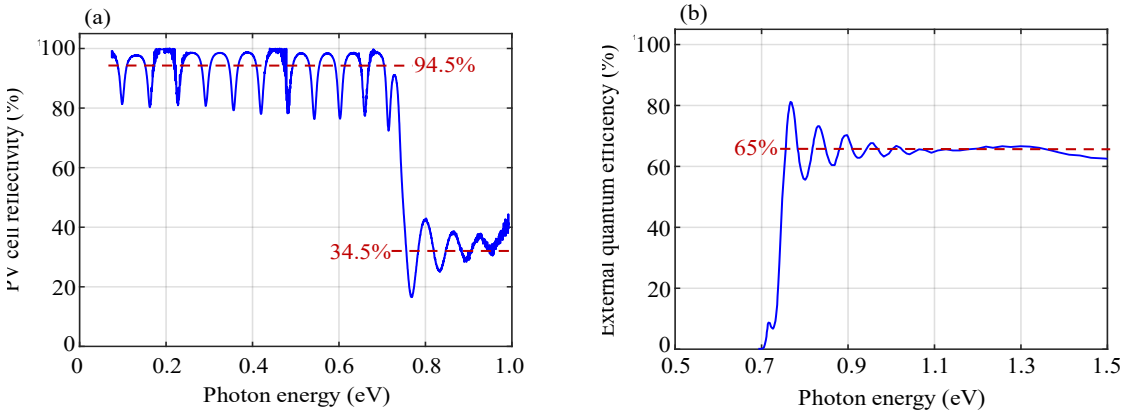

Fig. 3 Reflectivity and external quantum efficiency of one of the thermophotovoltaic cells. For this cell, sub-bandgap reflectivity is 94.5%. The above-bandgap reflectivity is the 34.5% Fresnel reflectivity at the air-semiconductor interface. The cell converts 65% of the above-bandgap incident photons to electron-hole pairs, as given by the external quantum efficiency on the right.

oscillations in Fig. 3(a) result from the expected thin-film interference in the semiconductor film. The average reflectivity for our devices, weighted by the Planck spectrum of thermal emission at 1200°C, for energies below the band edge, is 94.6%, corrected for the 0.5% systematic error in our FTIR setup. This is lower than the 98% reflectivity of the air-gold interface, due to the higher refractive index n=3.5 in the semiconductor, which reduces the critical angle at the semiconductor-gold interface. The measured reflectivity is 34.5% for energies

above the band edge, primarily due to Fresnel reflection at the air-semiconductor interface. These reflected photons undergo thermal regeneration in the emitter
The external quantum efficiency of the cell, shown in Fig. 3(b), is the fraction of photons incident on the front surface that are converted to electron-hole pairs and collected at the device terminals. The deviation of this value from 100% is primarily due to the lack of an anti-reflection coating on the photovoltaic cell.

Graphite emissivity measurement

The emitter, a thin graphite strip, is held in place by copper mounts on either side.

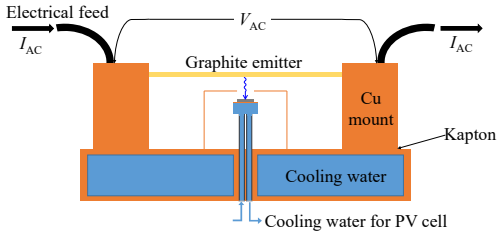

Fig.4 Power supply circuits for thermophotovoltaic efficiency calibration

Electrical power is injected into the graphite through the copper mount, resulting in Joule heating of the graphite emitter. The total electrical power injected into the copper mount-graphite system, at a steady emitter temperature T_s, is converted to heat in two different ways: radiation through graphite (due to high emissivity ε of the graphite) and Joule heating via the contact resistance (R_c) in the copper mount,

$$P_{\text{injected}} = V_{AC}I_{AC} = I_{AC}^2 R_C + A_{\text{emitter}}\varepsilon \int_0^\infty b_s(E,T_s)\cdot E dE, \quad (8)$$

where V_{AC}, I_{AC} are the RMS voltage and current injected into the mount-emitter system and A_{emitter} is the surface area of the emitter (98mm. ×14mm.). At a given emitter temperature T_s with known values of the V_{AC} and I_{AC}, the only unknowns in Eq (8) are the contact resistance R_c and emissivity ε. Hence, we can construct a system of equations with two closely spaced emitter temperatures (to reduce the effect from the temperature dependence of R_c) using Eq (8), and then solve for both R_c and ε. We measure an emissivity ε= 0.91 for graphite, consistent with reported values from Neuer[5].

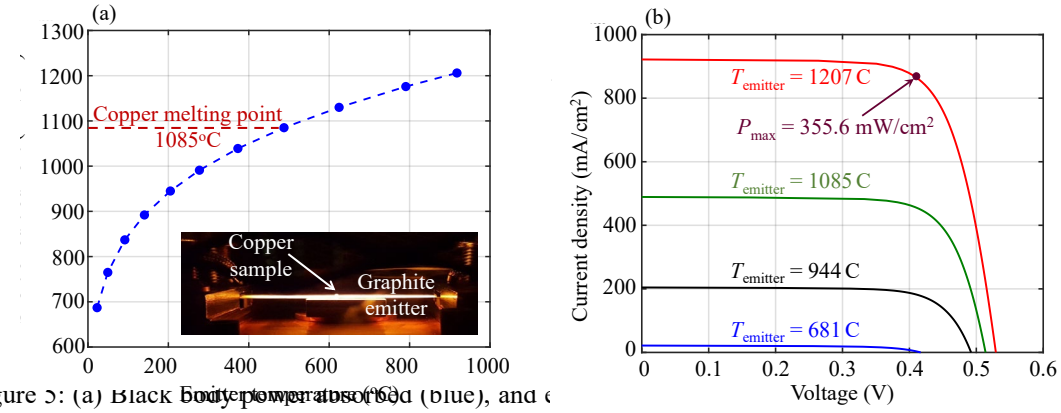

Figure 5: (a) Black body power absorbed (blue), and e cell.
(b) Thermophotovoltaic efficiency at different emitter temperatures. The maximum efficiency is 29.1% at an y

Fig. 6 Calibrating graphite emitter temperature by means of short circuit current measurement. In the first step, short-circuit current is at a reference temperature T=1085°C, the melting point of copper, on top of the graphite strip emitter, as shown with the inset in (a). The short circuit current in (b) calibrates temperatures at T≠1085C from the corresponding black body spectra at each temperature.

Results

We monitor the electrical power extracted from the thermophotovoltaic cell at the corresponding temperatures. The current voltage response of the thermophotovoltaic cell is shown in Fig. 6(b). The emitter temperature T_s and the electrical power generated $P_{electrical}(T_s)$, are steps toward the thermophotovoltaic cell efficiency $\eta(T_s) \equiv P_{electrical}(T_s)/P_{absorbed}(T_s)$.

The total radiant power absorbed at different emitter temperatures and the corresponding electric power generated is given in Fig. 5(a). The TPV conversion efficiency, the ratio between the two, is shown in Fig. 5(b), reaching a maximum of 29.1%, at 1207°C. Our result is compared with results from Wernsman et. al.[6], where they used similar emitter temperature ranges, with a corresponding photovoltaic cell bandgap =0.63eV. We get similar efficiency as Bechtel at 1039°C (peak efficiency in Bechtel's experiment), even though our cells are not optimized for operation at that temperature. This is due to two key improvements of our device compared to previous results, (*i*) the reflectivity of our mirror reached 94.6% versus 90% in prior work, and (*ii*) we have a better match of material bandgap to the Planck spectrum, leading to superior performance.

Although we achieved a new record for thermophotovoltaic cell efficiency (29.1%), and we see a pathway towards higher efficiencies, to translate this into a complete system would require further work on furnaces, combustion product circulation, thermal management, geometrical view factor, etc.

Error Analysis

Now we describe the accuracy of our efficiency calibration using both the procedures.

External Quantum Efficiency Based Approach

The thermophotovoltaic power efficiency is the ratio of $P_{electrical}$, the electrical power generated by the cell, to $P_{absorbed}$, the power absorbed by the cell. Since $P_{electrical}$ is measured with a high-precision source meter, the error in efficiency is dominated by $P_{absorbed}$. Hence, according to Eq. (2), the error arises from uncertainties in the measurement of graphite emissivity (ε), the cell absorptivity (1-R), and the emitter temperature, the last of which leads to an error in the Planck radiance (b_s). However, any uncertainty in emissivity is canceled by an equal and opposite change in the value of view factor F_{ef}, from Eq. (1)-(2). Hence the TPV efficiency uncertainty can be expressed through RMS addition as:

$$\frac{\triangle\eta}{\eta} = \sqrt{\left(\frac{\triangle a}{a}\right)^2 + \left(\frac{\triangle b_s}{b_s}\right)^2} \quad (9)$$

The absolute uncertainty in absorptivity $\triangle a$ ($\equiv\triangle R$) is 0.2%, due to statistical error in the measurement. The average absorptivity a is weighted by the incident Planck power spectrum at every temperature. For T_s = 1207°C, the average absorptivity is 14.46%, resulting in a relative error $\left(\frac{\triangle a}{a}\right)$= 0.014 for absorptivity.

The Planck spectrum at any given emitter temperature is determined from the measurement of short-circuit current, as given in Eq. (1). Since the current can be measured very accurately, the uncertainty in measuring b_s is dependent on the uncertainty of the EQE measurement:

$$\frac{\triangle b_s}{b_s} = \frac{\triangle \mathrm{EQE}}{\mathrm{EQE}} \quad (10)$$

The EQE was measured with 0.5% absolute accuracy, due to random error. This is further validated by the measurement of the open-circuit voltage in our experiment. The measured open-circuit voltage implies good material quality, along with a long diffusion length. This implies ~99% internal quantum efficiency of the photovoltaic cell. The average EQE for our devices is 65%, resulting in $\left(\frac{\triangle \mathrm{EQE}}{\mathrm{EQE}}\right)$ =0.008. Combining Eq. (S2) and (S3), we find a relative uncertainty $\frac{\triangle\eta}{\eta}$ =1.6% in our measured thermophotovoltaic efficiency, resulting in an absolute error of 29.1×.016=0.4%.

Internal Quantum Efficiency Based Approach

The accuracy of this method depends largely on temperature calibration using the melting point of copper and then convolving the corresponding black-body spectrum with the measured short circuit current. The reduction in short circuit current relative to the full black-body spectrum is accounted for by the emissivity-solid angle factor, εF_{eff}. We obtain this emissivity-solid angle factor by measuring the short-circuit current and the internal quantum efficiency.

The thermophotovoltaic efficiency is the ratio of electrical power generated by the thermophotovoltaic cell, to the thermal power absorbed by the cell. We measure the electrical power generated by the thermophotovoltaic cell very precisely with a Keithley 2400 source meter (with nanovolt precision). As such, the error in our efficiency measurement is entirely due to the error in the estimation of $P_{absorbed}$ with $\delta\eta/\eta=|\delta P_{absorbed}/P_{absorbed}|$.

The absorbed power at emitter temperature T_s depends on the Planck spectrum $b_s(E, T_S)$, the spectral absorptivity $\{1\text{-}R(E)\}$, and the internal quantum efficiency C, as shown in Eq. (6). We now show how each of these physical parameters affects the accuracy of thermophotovoltaic efficiency measurement.

Once the temperature is well-defined using the short-circuit current, we can know the Planck spectrum $b_s(E, T_s)$ accurately. The uncertainty in measuring $P_{absorbed}$ then depends entirely on the accuracy of measuring R_{below}, $R_{above,}$ and C.

The electrical power was measured very accurately with a nano voltmeter. As such, the error in our efficiency measurement is solely due to the error in the estimation of $P_{absorbed}$, $\delta\eta/\eta=|\delta P_{absorbed}/P_{absorbed}|$.

We can substitute εF_{eff} in Eq. (3) from Eq. (4') as follows:

$$P_{absorbed} = \frac{J_{sc}(T_s)}{q} \times \frac{\int_0^\infty \{1 - R(E)\} b_s(E, T_s) dE}{\int_0^\infty \{1 - R(E)\} C(E)\, b_s(E, T_s)/E \cdot dE} \qquad (11)$$

We can write $EQE = C\times\{1\text{-}R(E)\}$, where internal quantum efficiency C expresses the probability of an absorbed photon to generate electron-hole pair. C is 0 below the bandgap E_g. Separating the super-bandgap and sub-bandgap parts of the integral in Eq. (11), we get,

$$P_{absorbed} = \frac{J_{sc}(T_s)}{q} \times \frac{\int_0^{E_g} \{1 - R(E)\} b_s(E, T_s) dE}{\int_{E_g}^\infty \{1 - R(E)\} C(E)\, b_s(E, T_s)/E \cdot dE} + \frac{J_{sc}(T_s)}{q} \times \frac{\int_{E_g}^\infty \{1 - R(E)\} b_s(E, T_s) E dE}{\int_{E_g}^\infty \{1 - R(E)\} C(E)\, b_s(E, T_s)/E \cdot dE} \qquad (12)$$

At a given temperature, $b_s(E, T_s)$ and $J_{sc}(T_s)$ are precisely known. For the ease of derivations, let's define R_{below}, R_{above}, $\acute{C}$ to denote the sub-bandgap reflectivity, super-bandgap reflectivity, and the internal quantum efficiency respectively, all the terms being spectrally averaged within the limits of the respective integral. We can now re-write Eq. (12) as:

$$
\begin{aligned}
P_{absorbed} = & \frac{J_{sc}(T_s)}{q} \times \frac{(1-R_{below})\int_0^{E_g} b_s\,(E,T_s)dE}{(1-R_{above})\acute{C}\int_{E_g}^{\infty} b_s\,(E,T_s)/E\cdot dE} + \frac{J_{sc}(T_s)}{q} \\
& \times \frac{(1-R_{above})\int_{E_g}^{\infty} b_s\,(E,T_s)dE}{(1-R_{above})\acute{C}\int_{E_g}^{\infty} b_s\,(E,T_s)/E\cdot dE} \\
= & \frac{J_{sc}(T_s)}{q} \times \frac{(1-R_{below})\int_0^{E_g} b_s\,(E,T_s)dE}{(1-R_{above})\acute{C}\int_{E_g}^{\infty} b_s\,(E,T_s)/E\cdot dE} + \frac{J_{sc}(T_s)}{q} \\
& \times \frac{\int_{E_g}^{\infty} b_s\,(E,T_s)dE}{\acute{C}\int_{E_g}^{\infty} b_s\,(E,T_s)/E\cdot dE}
\end{aligned} \tag{13}
$$

Now, we can take partial derivatives with respect to R_{below}, R_{above}, $\acute{C}$, and P_{absorbed} on both sides of Eq. (13). Before we do that, let us call the first term on the RHS of Eq. (13) as A and the second term as $\dot{B}$. As such, $P_{\text{absorbed}} = A+\dot{B}$. Now, taking the derivatives on both sides of Eq. (13), we get,

$$
\begin{aligned}
\partial P_{absorbed} = & -\frac{\partial R_{below}}{(1-R_{below})}(P_{absorbed}-\dot{B}) + \frac{\partial R_{above}}{(1-R_{above})}(P_{absorbed}-\dot{B}) \\
& - \frac{\partial \acute{C}}{\acute{C}}(P_{absorbed}-\dot{B}) - \frac{\partial \acute{C}}{\acute{C}}(P_{absorbed}-A) \\
= & -\frac{\partial R_{below}}{(1-R_{below})}(P_{absorbed}-\dot{B}) + \frac{\partial R_{above}}{(1-R_{above})}(P_{absorbed}-\dot{B}) \\
& - \frac{\partial \acute{C}}{\acute{C}}(2\times P_{absorbed}-\dot{B}-A) \\
= & -\frac{\partial R_{below}}{(1-R_{below})}(P_{absorbed}-\dot{B}) + \frac{\partial R_{above}}{(1-R_{above})}(P_{absorbed}-\dot{B}) \\
& - \frac{\partial \acute{C}}{\acute{C}}P_{absorbed}
\end{aligned} \tag{14}
$$

As such, the root-mean-square error is,

$$
\begin{aligned}
\partial P_{absorbed} = & \sqrt{\left|\frac{\partial R_{below}}{(1-R_{below})}(P_{absorbed}-\dot{B})\right|^2 + \left|\frac{\partial R_{above}}{(1-R_{above})}(P_{absorbed}-\dot{B})\right|^2 + \left|\frac{\partial \acute{C}}{\acute{C}}P_{absorbed}\right|^2} \\
= & \sqrt{\left|\frac{\partial R_{below}}{(1-R_{below})}\right|^2 (P_{absorbed}-\dot{B})^2 + \left|\frac{\partial R_{above}}{(1-R_{above})}\right|^2 (P_{absorbed}-\dot{B})^2 + \left|\frac{\partial \acute{C}}{\acute{C}}P_{absorbed}\right|^2}
\end{aligned}
$$

$$\frac{\partial P_{absorbed}}{P_{absorbed}} = \sqrt{\left|\frac{\partial R}{a_{below}}\right|^2 (P_{absorbed} - \dot{B})^2 + \left|\frac{\partial R}{a_{above}}\right|^2 (P_{absorbed} - \dot{B})^2 + \left|\frac{\partial C}{C} P_{absorbed}\right|^2}$$

$$= \sqrt{\left|\frac{\partial R}{a_{below}}\right|^2 (1-B)^2 + \left|\frac{\partial R}{a_{above}}\right|^2 (1-B)^2 + \left|\frac{\partial C}{C}\right|^2}$$

$$\frac{\partial \eta}{\eta} = \sqrt{\left(\left|\frac{\partial R}{a_{below}}\right|^2 + \left|\frac{\partial R}{a_{above}}\right|^2\right) f_{abs,below}{}^2 + \left|\frac{\partial C}{C}\right|^2} \quad (15)$$

This gives us the expression of relative error of the absorbed power, and in turn the relative error in thermophotovoltaic efficiency. Here, we use $\delta R_{\text{below}} = \delta R_{\text{above}} = \delta R$, the systematic error in our FTIR measurement. Also, a denotes the absorptivity, with the subscript indicating the relevant part of the spectrum. From the previous section, we know $C = \acute{C}$, as quantum efficiency does not vary with the emitter temperature for our experiment. Finally, we use $B = \dot{B}/P_{\text{absorbed}} = 1 - f_{\text{abs, below}}$. The temperature-dependent factor $f_{\text{abs below}}$ tell us the fraction of the thermal radiation absorbed by the cell that is below the bandgap.

An additional contribution to δR is due to scattering from the electrical grid lines, on top of the thermophotovoltaic cells, as shown in Fig. 2. The electrical grid lines on the top of the thermophotovoltaic cell are 5um wide and 200μm apart. We measure the reflectivity with a 150μm spot size, in between the grid lines. The reflectivity on the Au grid lines is 98%, but at the air-semiconductor interface, the net reflectivity is 94.5%. From linear interpolation, the front surface reflectivity can be 94.6%, including the grids. We make this interpolation taking 2.5% front surface coverage by the gridlines into account. As such, our measured reflectivity has an additional uncertainty of 0.1%. This results in net reflectivity uncertainty of 98±0.3%.

We can measure the errors in the internal quantum efficiency δC. We obtain C=98.9% from the measured open-circuit voltage, as discussed in the appendix. Given the 50% uncertainty in the diffusion length, the uncertainty on our internal quantum efficiency is 98.9±0.9%.

Now using the measured δC and δR we can calculate the efficiency uncertainty $\delta\eta$ given by Eq. (15). The relative uncertainty $\delta\eta/\eta$ as a function of emitter temperature is shown in Fig. 7. As the emitter temperature increases, more photons are emitted above the band edge than below. The error is given by $\delta R \times f_{\text{abs, below}}$ decreases, while the signal $1\text{-}R_{\text{above}}$ increases with increasing emitter temperature. Therefore, the signal-to-noise ratio improves with temperature. This is shown in Fig. 7. At 1207°C, the calibrated thermophotovoltaic efficiency is 29.1%, with an uncertainty of 29.1±0.6%. In the external quantum efficiency-based approach, the uncertainty was 29.1±0.4%. However, the previous calibration depended on the calibration of emitter temperature using short-circuit current and external quantum efficiency and then convolving the Planck spectrum with the thermophotovoltaic

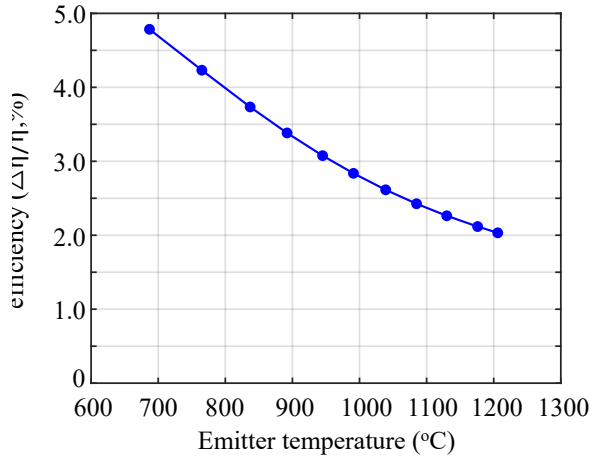

Fig. 7: Accurate calibration of record thermophotovoltaic efficiency. The uncertainty in efficiency is mainly determined by the relative uncertainty of the sub-bandgap reflectivity. As the emitter temperature increases, more photons are emitted above the band-edge than below. This results in a higher signal-to-noise ratio with increasing temperature.

cell absorptivity. Using a different approach based on the carrier collection efficiency, we arrive at the same efficiency, without relying on a separate measurement of external quantum efficiency.

We can compare the accuracy of our method to the traditional calorimetric method. Precise calorimetry requires complete minimization of parasitic heat absorption to achieve any reasonable accuracy, which can be challenging. In our approach, we rely on the electrical measurement of short-circuit current and open-circuit voltage, and optical measurement of reflectivity. All of these measurements are routine. Thus we can potentially achieve better accuracy compared to calorimetric measurement of thermophotovoltaic cell efficiency.

The thermophotovoltaic cells were scanned 200 times to reduce the corresponding random error in sub-bandgap reflectivity. The efficiency calibration using the

copper melting point for temperature, and then convolving the corresponding black-body spectrum with the measured short-circuit current, provides a simple and precise absolute calibration method in thermophotovoltaics.

Pathway for future improvements

We now project further improvements in thermophotovoltaic efficiency, as key device and chamber parameters improve. The key device parameters are the internal luminescence efficiency η_{int}, series resistance R_s, and the rear mirror reflectivity R_{rear}=94.6%. A poor η_{int} is linked to significant loss of open-circuit voltage in the photovoltaic cell[3]. From our current voltage curves, we extract a series resistance $R_s = 0.43\Omega$ and estimate $\eta_{int} \sim 82\%$, corresponding to $\eta_{ext} \sim 3.5\%$. Based on these values of η_{int}, $R_{rear,}$ and R_s, we project the thermophotovoltaic efficiency of our cell at different temperatures (solid blue line in Fig. 8) and also compare it with the experimentally measured values (blue dots). The efficiency begins to diminish at emitter temperatures >1350°C. Series resistance limits the performance of the device in that temperature range, where the brighter illumination gives rise to a larger short-circuit current, and therefore larger resistive voltage drop. The detailed procedure for estimating η_{int} and R_s from the current voltage data is given in the supplementary section.

We measure the heat to the electricity conversion efficiency of the photovoltaic cell in our setup. Our setup differs from a thermophotovoltaic system in a full chamber in two key factors: (1) the geometric view factor, which should be unity in the full chamber, and (2) the series resistance, which should be limited by the inherent series resistance of the device. The latter can be achieved via interconnect metallization in large-scale devices. High series resistance penalizes the cell's fill factor due to a resistive voltage drop. In our case, the device had an inherent $R_s \sim 0.1\Omega$, but we had an excess 0.33Ω introduced by the wire bonds. If these technical difficulties are resolved we project that such system, using a photovoltaic cell identical to ours, would have a power conversion efficiency of 33.6% at 1207°C. This projection is shown by the red line in Fig. 8.

The projected effect of improved sub-bandgap reflectivity, from an average value of 94.6% to 98% is shown by the green curve in Fig. 8. This improvement in reflectivity can be obtained by adding a layer of low refractive index dielectric between the rear gold layer and the semiconductor[7].

Improving the material quality of the photovoltaic device, which we parameterize with the internal luminescence efficiency η_{int}, leads to an enhancement in both operating and open-circuit voltages. The internal luminescence efficiency of InGaAs is mainly affected by defect-mediated Shockley-Read-Hall recombination and, to a

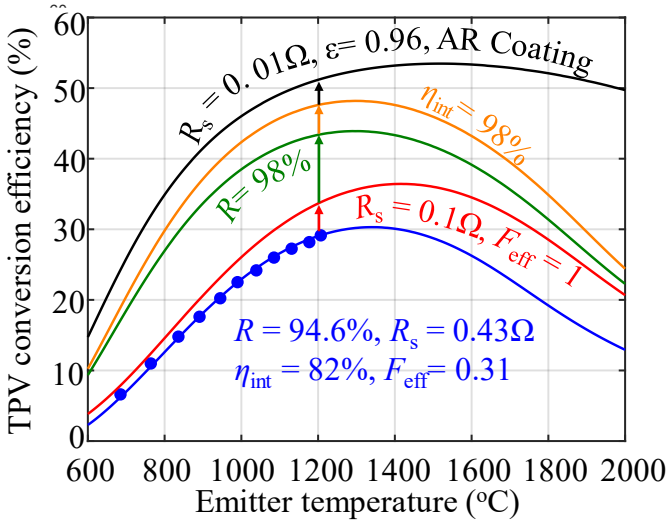

Figure 8: Projection of thermophotovoltaic efficiency. Effects of device and material quality, emitter as well as chamber geometry on the system efficiency is illustrated. With the realistic projection of improvement in these key device and chamber parameters, more than 50% thermophotovoltaic conversion efficiency is possible.

lesser extent, by intrinsic Auger recombination. The best reported[Error! Bookmark not defined.] values for InGaAs films reached τ_{SRH} ~47μs, with a corresponding Auger coefficient ~8.1×10^{-29}cm^{6}s^{-1}. For our projection, we use a more moderate Shockley-Read-Hall lifetime τ_{SRH} ~ 10μs, ~ 2 orders of magnitude longer than the lifetime τ_{SRH} ~ 60ns in our device. This would increase the value of η_{int} to 98%. This improvement in the internal luminescence efficiency leads to a larger voltage in the photovoltaic cell, raising the thermophotovoltaic efficiency to ~48%, as shown by the orange curve in Fig. 8.

Further efficiency gains can be achieved using an anti-reflection coating, and by maximizing the emitter emissivity using silicon carbide as the emitter instead of graphite, since the former has an emissivity $\varepsilon = 0.96$ versus $\varepsilon = 0.90$ of the latter. This full set of improvements can lead to >50% power conversion efficiency in an InGaAs thermophotovoltaic system, as shown by the black line in Fig. 8.

Although we have achieved a new record for thermophotovoltaic cell efficiency (29.1%), to translate this into a full thermophotovoltaic system would require further

work on furnaces, combustion product circulation, thermal management, and other elements.

References

[1] For our calculations, we use an effective emissivity ε_{eff} instead of using the emissivity ε of graphite to take into account multiple reflections between the cell and the emitter. The effective emissivity, ε_{eff} is given by $\frac{\varepsilon}{1-R(E)(1-\varepsilon)}$, where the reflectivity spectrum, $R(E)$, changes sharply when transitioning to energies above the bandgap. The emissivity difference is $(\varepsilon_{\text{eff}}-\varepsilon)/\varepsilon = 5\%$, which leads to a shift of thermophotovoltaic efficiency from 29.7% to 29.1%.

[2] R. F. Pierret, Ch.10 in "Semiconductor Device Fundamentals," Pearson, 2011. The hyperbolic cosine can be extended by Taylor series to arrive at the expression.

[3] O. D. Miller, S. Kurtz, and E. Yablonovitch, Strong internal and external luminescence as solar cells approach the Shockley-Quiesser limit, IEEE J. Photovolt., 2 (3), 303–311 (2012).

[4] Electrical Properties of Gallium Indium Arsenide, http://www.ioffe.ru/SVA/NSM/Semicond/GaInAs/ebasic.html, online (Accessed July 2020).

[5] G. Neuer, "Spectral and total emissivity measurements of highly emitting materials," *Int. J. Thermophys.*, vol. 16, no. 1, pp. 257–265, Jan. 1995.

[6] B. Wernsman et al., "Greater than 20% radiant heat conversion efficiency of a thermophotovoltaic radiator/module system using reflective spectral control," *IEEE Trans. Electron Devices*, vol. 51, no. 3, pp. 512–515, Mar. 2004.

[7] D. Fan, T. Burger, S. McSherry, B. Lee, A. Lenert, and S. R. Forrest, "Near-perfect photon utilization in an air-bridge thermophotovoltaic cell," Nature, (September 2020).

3. Broadband Mirror for Thermophotovoltaics

From the previous section, we have shown the importance of a highly reflective mirror in improving the power conversion efficiency of thermophotovoltaics. We show the effects of improving mirror reflectivities on the power conversion efficiency of thermophotovoltaics in Fig. 1. Two things are more noticeable:

(i) There is an increasing return of efficiency when the mirror reflectivity improves, and

(ii) Efficiency boost is tremendous for temperatures<1000C.

We can explain the first observation as follows:

The open-circuit voltage in photovoltaic cells has seen tremendous benefits from luminescence extraction, over the last decade[1]. A highly luminescent photovoltaic

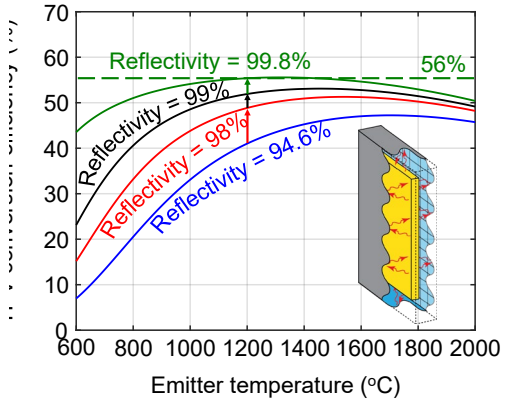

Fig. 1: Effect of mirror reflectivity on thermophotovoltaic efficiency.

cell requires minimization of material loss and improvement in photon extraction. In the limit of excellent material quality, the detailed balance is satisfied with emission from the front of the photovoltaic cell. The front-surface emission requires efficient luminescence extraction.

Both photon extraction and photon recycling can be improved through improvements in rear mirror reflectivity. An excellent mirror increases the density of photons inside the cell, by reflecting photons that otherwise be wasted. Reflection from the rear mirror gives the photons an additional chance to reach the front surface, in case the photon was not emitted previously. This helps photon extraction.

The rear mirror thus helps the thermophotovoltaic cells in two different ways. This results in the increasing returns relation of power conversion efficiency, with respect to the rear mirror reflectivity for thermophotovoltaics.

At a lower temperature of the emitters, for a fixed bandgap of the thermophotovoltaic cell, the dominant loss mechanism is either the mirror loss or the thermalization loss. As the mirror loss decreases with increasing mirror reflectivity, the limiting loss mechanism is then thermalization loss. This leads to the improvement noted by observation (ii).

As such, there is a tremendous benefit of every 1% improvement in reflectivity beyond 94%.

Broadband Mirrors: Past and Limitations

For broadband mirrors, the two most common solutions are either metal mirrors or distributed Bragg reflectors.

In our previous experiments, we have used a gold mirror. This resulted in 94.6% average reflectivity over the desired frequency spectrum. Although metals have quite a broadband reflectivity spectrum, the reflectivity is limited by intrinsic material losses of the metal itself. As such, better options are needed to improve the reflectivity beyond 94.6%. An alternative would be a dielectric-metal mirror, such as the one used by Lenert et. al.[2] with air as the dielectric. However, the spectral reflectivity is still limited to ~97%.

Distributed Bragg mirrors are alternating layers of high and low-refractive-index materials of fixed optical thickness. Successive interferences within each layer give rise to a very high reflectivity (as high as 99.99%). But this is limited to a relatively narrow frequency spectrum, defined by the optical thickness of the individual layers. While this is sufficient for lasers and light-emitting diodes, this is not sufficient for thermophotovoltaics. Figure 3. illustrates the problem.

Continuously chirped Bragg Mirror:

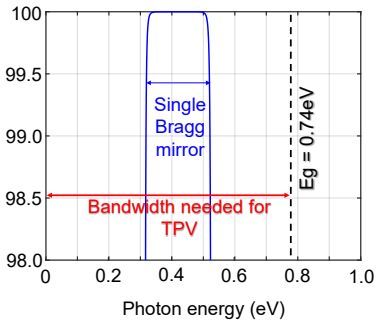

Figure 3: Thermophotovoltaics require mirrors with bandwidth 3 times greater than that can be achieved with distributed Bragg mirrors.

To circumvent this problem, modifications to DBR have been attempted. Instead of a fixed thickness of the dielectric layers, the layer thickness can be varied to obtain

broadband reflectivity. Each layer thickness corresponds to a different center frequency, and thus a broader reflectivity spectrum can be obtained, as shown in Fig. 4 (a). However, this approach has an inherent challenge. The reflections from the layers can interfere destructively at certain wavelengths, giving rise to 'nulls' in the reflectivity spectrum (Fig. 4 (b)). The spectral location of the null is hard to control by hand, due to the near-random nature of the interference in this mirror. As such, they can penalize the reflectivity spectrum.

As such, obtaining a high reflectivity, over a broad frequency spectrum necessitates a precise control of the location of the nulls. As such, an optimization procedure is needed.

Optimization of Broadband Mirrors:

Our objective is to achieve mirrors, with reflectivity ≥99%, when averaged over polarization, incident angle, and photon energies over the relevant incident thermal spectrum. We can express this average reflectivity as the figure-of-merit in our optimization as follows:

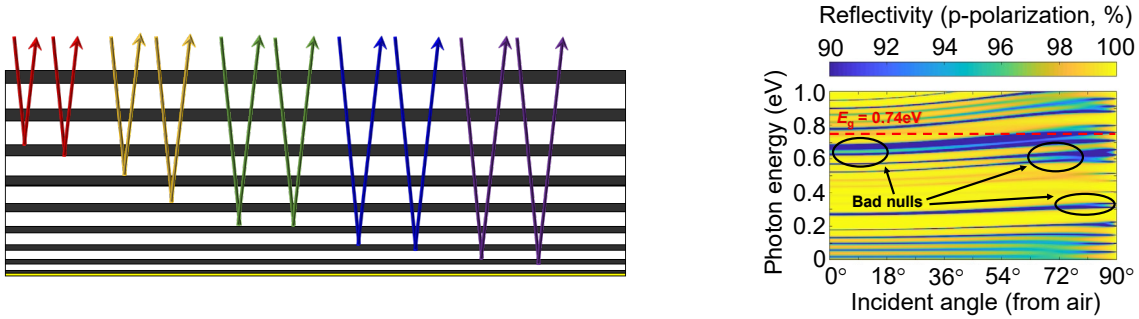

Figure 4: Continuously chirped mirrors and null. Continuously chirped mirror (a) can reflect a broader frequency spectrum, compared to the distributed Bragg mirror. However, presence of nulls in the reflectivity spectrum (b) reduces the average reflectivity.

$$FOM = \frac{2\pi \int_0^{\pi/2} \int_0^{E_g} \frac{1}{2}(|r_s(E,\theta)|^2+|r_s(E,\theta)|^2) b_s(E,T_s) sin(\theta)\, cos(\theta) dE d\theta}{2\pi \int_0^{\pi/2} \int_0^{E_g} b_s(E,T_s) sin(\theta)\, cos(\theta) dE d\theta} \quad (1)$$

In Eq. (1), r_s and r_p are the complex reflectivities for the mirror for s and p polarization of incident light, bs (E, T_s) is the power flux emitted by the thermal emitter at T_s (in units of W/m^2/Str), and E_g is the bandgap energy of the thermophotovoltaic cell. The factor of sin(θ) comes from the spherical differential, and cos(θ) accounts for a Lambertian photon flux from the thermal emitter. The azimuthal angle θ variation is taken from 0 to π/2 since we are interested in measuring the reflectivity, a surface property.

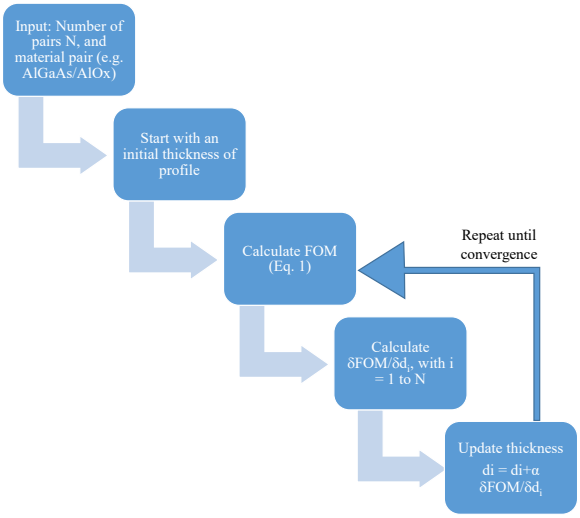

Figure 5: Optimization procedure for broadband mirror in thermophotovoltaics

For a given material system of Bragg mirror (such as Si/SiO_2 or $AlGaAs/ AlO_x$), our only degrees of freedom for optimization are (i) how many alternating layers of low and high-refractive-index material we want to use in the mirror, and (ii) the thickness of each layer. We can then envision an optimization program that takes the number of alternating layers of low and high-refractive-index materials (i.e. the number of pairs in the mirror, N) as input. The program then optimizes the thickness of each layer to achieve maximum reflectivity. Thus, the optimizer will calculate the $\delta FOM/\delta d_i$, with i = 1 to N, and will update the thickness to maximize the FOM. This is illustrated in the flow diagram in Fig. 5.

From Fig. 5, we need two functions from the optimization problem, a way to calculate the FOM and calculate the derivative of the FOM, with respect to the thickness of each layer d_i. For the FOM given by Eq. (1), we need to know the complex reflectivities r_p and r_s for the broadband mirror. For a 1-dimensional layer stack, this is easy to obtain from a transfer-matrix method simulation. The FOM derivative $\delta FOM/\delta d_i$ is difficult to obtain. For optimizing photonic structures, methods such as the adjoint method, automatic differentiation, neural networks, etc. have been used. Here, we show that for the case of 1-dimensional mirrors, we can obtain the derivative directly from another transfer-matrix method. This lets us calculate the exact derivatives (thus greater accuracy), and massively parallelize the computation.

Derivative of Figure of Merit

In this section, we'll elaborate on the derivative of FOM with respect to the thickness d_i of a layer i. We can write that derivative as follows:

$$\frac{\delta FOM}{\delta d_i} = \frac{2\pi \int_0^{\pi/2} \int_0^{Eg} \frac{1}{2}\left(\frac{\delta|r_S(E,\theta)|^2}{\delta d_i} + \frac{\delta|r_p(E,\theta)|^2}{\delta d_i}\right) b_s(E,T_S) sin(\theta)\, cos(\theta) dE d\theta}{2\pi \int_0^{\pi/2} \int_0^{Eg} b_s(E,T_S) sin(\theta)\, cos(\theta) dE d\theta}$$

$$= \frac{2\pi \int_0^{\pi/2} \int_0^{Eg} \frac{1}{2}\left(2r_s^*(E,\theta)\frac{\delta\{r_S(E,\theta)\}}{\delta d_i} + 2r_p^*\frac{\delta\{r_p(E,\theta)\}}{\delta d_i}\right) b_s(E,T_S) sin(\theta)\, cos(\theta) dE d\theta}{2\pi \int_0^{\pi/2} \int_0^{Eg} b_s(E,T_S) sin(\theta)\, cos(\theta) dE d\theta}$$

As such, to calculate the derivative of FOM with respect to layer thickness d_i, we need to compute the derivative of the complex reflection coefficient $r_p(E,\theta)$ and $r_s(E,\theta)$ with respect to d_i. We'll describe the procedure in the next section.

Derivative of Thickness from Transfer Matrix Method

We'll show the calculation for p-polarization only. The procedure will be the same for s-polarization. We'll drop the E and θ dependence for simplicity. For a multi-layered structure, we can express the reflectivity as:

$$r_p = \frac{M_{21}}{M_{11}}$$

$$\text{where } \boldsymbol{M} = \begin{bmatrix} M_{11} & M_{12} \\ M_{21} & M_{22} \end{bmatrix} = \boldsymbol{T}_{1,2} \prod_{i=2}^{i=N-1} \boldsymbol{P}_i(d_i) \boldsymbol{T}_{i,i+1} \quad (2)$$

In Eq. (2), we have the matrices $\boldsymbol{P}$ and $\boldsymbol{T}$ as:

$$\boldsymbol{P}_i(d_i) = \begin{bmatrix} exp(-jk_i d_i) & 0 \\ 0 & exp(jk_i d_i) \end{bmatrix}$$

$$\boldsymbol{T}_{i,i+1} = \frac{1}{2}\begin{bmatrix} \frac{k_{i+1}n_i}{k_i n_{i+1}} + \frac{n_{i+1}}{n_i} & \frac{k_{i+1}n_i}{k_i n_{i+1}} - \frac{n_{i+1}}{n_i} \\ \frac{k_{i+1}n_i}{k_i n_{i+1}} - \frac{n_{i+1}}{n_i} & \frac{k_{i+1}n_i}{k_i n_{i+1}} + \frac{n_{i+1}}{n_i} \end{bmatrix}$$

Here $k_i = 2\pi n_i \cos(\theta_i)/\lambda$. As such the only thickness-dependent term in Eq. (2) is the propagation matrix $\boldsymbol{P}$.

We can take the derivative of the complex reflection coefficient rp as follows:

$$\frac{\delta r_p}{\delta d_i} = \frac{M_{11}\frac{\delta M_{21}}{\delta d_i} - M_{21}\frac{\delta M_{11}}{\delta d_i}}{M_{11}^2}$$

We can obtain the derivatives of the matrix elements of $\boldsymbol{M}$ in the following manner:

$$\frac{\delta \boldsymbol{M}}{\delta d_i} = \begin{bmatrix} \frac{\delta M_{11}}{\delta d_i} & \frac{\delta M_{12}}{\delta d_i} \\ \frac{\delta M_{21}}{\delta d_i} & \frac{\delta M_{22}}{\delta d_i} \end{bmatrix} =$$

$$\boldsymbol{T}_{1,2}\boldsymbol{P}_2(d_2)\boldsymbol{T}_{2,3}\boldsymbol{P}_3(d_3)\ldots\boldsymbol{T}_{i-1,i}\ \frac{\delta \boldsymbol{P}_i(d_i)}{\delta d_i}\boldsymbol{T}_{i,i+1}\cdots\boldsymbol{T}_{N-1,N}$$

As such we need a derivative only for the propagation matrix of layer i. The derivative of $\boldsymbol{P}_\mathrm{i}(d_\mathrm{i})$ with respect to the layer thickness d_i can be written as:

$$\frac{\delta \boldsymbol{P}_i(d_i)}{\delta d_i} = jk\begin{bmatrix} -exp(-jk_i d_i) & 0 \\ 0 & exp(jk_i d_i) \end{bmatrix} = exp(j\frac{\pi}{2})jk\begin{bmatrix} exp(j\frac{\pi}{2})exp(-jk_i d_i) & 0 \\ 0 & exp(-j\frac{\pi}{2})exp(jk_i d_i) \end{bmatrix}$$

$$= -k\begin{bmatrix} exp\{-j(\frac{2\pi n_i cos(\theta_i)}{\lambda}d_i - \frac{2\pi n_i cos(\theta_i)}{\lambda}\frac{\lambda}{4n_i cos(\theta_i)})\} & 0 \\ 0 & exp\{j(\frac{2\pi n_i cos(\theta_i)}{\lambda}d_i - \frac{2\pi n_i cos(\theta_i)}{\lambda}\frac{\lambda}{4n_i cos(\theta_i)})\} \end{bmatrix}$$

This final expression gives us an interesting insight. It tells us the derivative of the $\boldsymbol{P}_\mathrm{i}$ matrix is another propagation matrix, but the layer thickness changed by $\frac{\lambda}{4n_i cos(\theta_i)}$. Thus, we can envision the derivative calculation as the backward simulation of the inverse design. In the forward simulation, we calculate the r_p for the given d_i, using the transfer matrix method. In the inverse simulation, we calculate $\delta r_\mathrm{p}/\delta d_\mathrm{i}$ by another transfer matrix method, with d_i replaced with $d_i - \frac{\lambda}{4n_i cos(\theta_i)}$.

Initial Point

Any local optimization, such as ours, is very sensitive to the initial point (mirror thickness profile in our case). A physically meaningful initial point can help to avoid spurious local minimum in the result [4]. We use a continuously chirped thickness profile, as the starting point for the design. As explained previously, the continuous chirp structure provides a physically meaningful structure for a broadband mirror (Fig. 4 (a)), by reflecting each color of light at various depths. However, the incoherent additions of the rays coming from the continuously chirped structure cause the appearance of nulls. These nulls are thus hard to control due to the random nature. The average reflectivity goes down. However, the inverse design procedure can go through successive iterations to remove the nulls.

RESULTS

Here we show the results of optimization with our proposed inverse design approach. We use the number of pairs as an input to the program and use the spectrally averaged refractive index 3.5 (AlGaAs) and 1.6 (AlOx) for the mirror

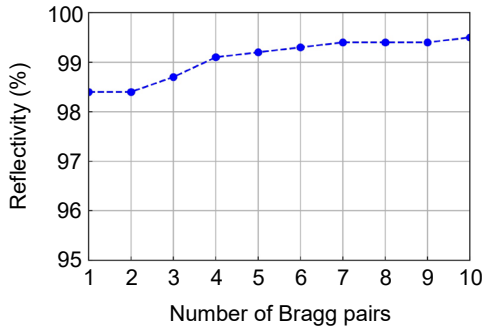

Figure 6: Optimized reflectivity as a function of number of pairs in the mirror stack

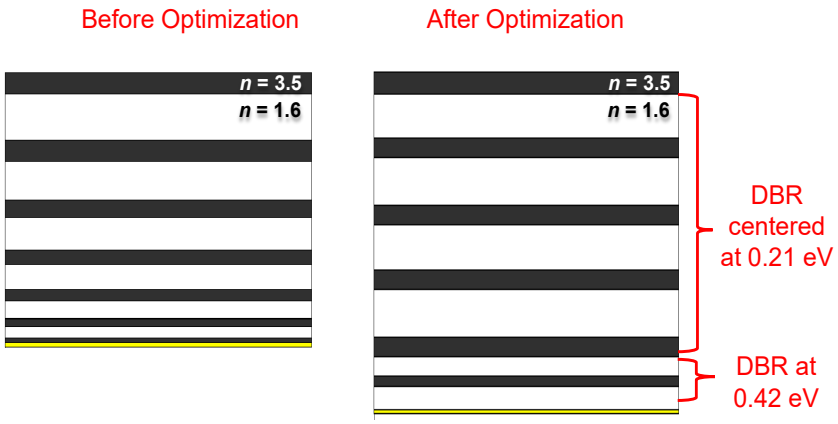

Figure 7: Thickness profile of mirror, before and after optimization. We start the optimization with a continuously chirped structure. The optimized structure in all cases, is a stepwise chirped structure, as shown on the right for a six-paired mirror.

layers. The top layer is taken to be InP (0.5μm thickness), and the structure is capped by Gold at the end, with an average refractive index of 0.5+11j.

The spectrally averaged reflectivity, as shown in Fig. 3, increases as the number of Bragg pairs is increased. This is expected, similar to distributed Bragg mirrors used

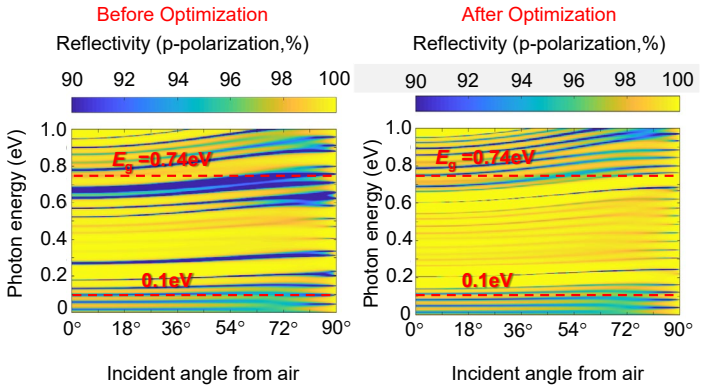

Figure 8: Reflectivity, before and after optimization. The nulls in the reflectivity spectrum are removed as a result of the optimization. This improves the average reflectivity. The red line indicates the region of the spectrum where optimization was performed.

for lasers. However, the average reflectivity (0.1-0.74 eV, ~3 octave) reaches >99% for pair numbers ≥ 4.

The final optimized structure, in all cases, is very different from the continuously chirped structure. For example, for a 6-paired mirror, the final structure was two distributed Bragg mirrors in tandem. We can think of it as a stepwise chirp, in contrast to the continuous chirp that we started the optimization with.

The optimization also removes the nulls from the continuously chirped structure, as shown in Fig. 8. As such, the average reflectivity improves.

Effect of Material Loss

Now, we show the mirror reflectivities including the losses in the oxide layers of the mirror. Most oxide dielectrics show phonon absorption. We show the effect of this material absorption in Fig. 9. This is for a mirror with InP superstrate with 350μm thickness. The materials for the mirror have refractive indices 3.5 and 1.6.

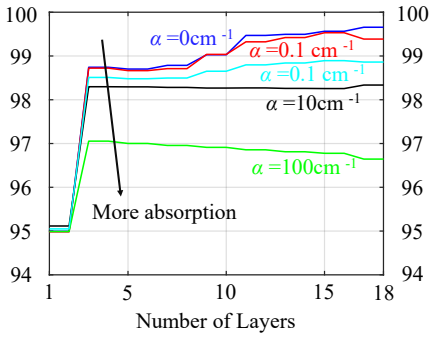

Figure 9: Mirror reflectivities for the optimized mirror for different absorption coefficients. The refractive indices of the low and high index of the mirror is 1.6 and 3.5, respectively. The superstrate is InP (n = 3.5), with 350μm thickness.

Next, we show the reflectivity of a seven-layered Si-SiO_2 mirror, the average reflectivity from 0.16-0.74eV and 0°-90° incident angles is 99%. The experimental result in Fig. 10 is measured at 34° incident angle from the air.

Conclusion

We show a new method for designing broadband mirrors using the transfer matrix method and Fresnel propagation. We design a stepwise chirped structure that removes destructive interference for the low-energy photons in thermophotovoltaics thereby improving the reflectivity. The broadband mirrors thus can push the efficiencies of thermophotovoltaics above the internal combustion engines.

References

[1] O. D. Miller, S. R. Kurtz, and E. Yablonovitch, "Strong internal and external luminescence as solar cells approach Shockley-Queisser limits," IEEE Journal.

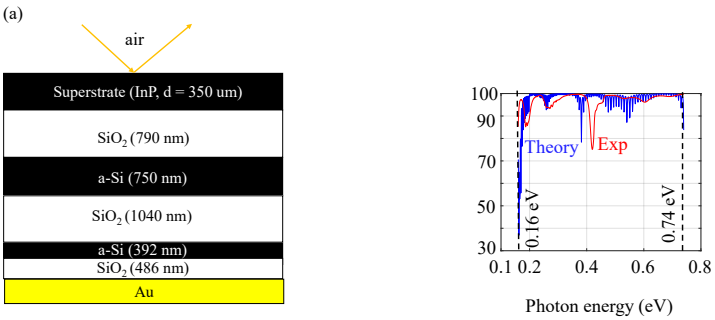

Figure 10: 99% reflectivity over 2.5 octave frequency spectrum. The experimental measurement follows the theoretical reflectivity spectrum closely. When the data is projected from 0°-90° incident angles from air, the average reflectivity is 99%.

Photovolt. (2012).

[2] Fan D., Burger T., McSherry S., Lee B., Lenert A., and Forrest S. R., "Near-perfect photon utilization in an air-bridge thermophotovoltaic cell," Nature 586, 237-241 (2020).

[3] A. Michaels, "Inverse design of near-unity efficiency perfectly vertical grating couplers," Opt. Exp. 26 (4), 4766-4779 (2018).

4. Open-circuit Voltage in Poorly Luminescent Solar Cells

Single-junction solar cell efficiency has jumped closer to the detailed-balance limit over the last decade[1]. GaAs solar cells are largely responsible for this efficiency increase. Proper photon management in high-quality GaAs has been a key driver. This improvement in efficiency is dependent on improving the open-circuit voltage from the cell. The concept of current is easier to understand. Better photon absorption and charge extraction lead to higher short circuit currents in the solar cell. The concept of voltage is more involved. It is precisely the understanding of the underlying physics of voltage that has been the key to record GaAs solar cell efficiencies [1, 2].

In an ideal material, the detailed balance dictates the equality of emission and absorption in any photochemical process [3, 4]. Miller et. al. [5] thus pointed out that solar cells should be counterintuitively designed, to maximize photon emission at open-circuit. Thus luminescence extraction has been identified as a key mechanism for record-breaking efficiencies in GaAs solar cells. The mantra—a good solar cell is also a good LED—has been a driving force behind designing solar cells for efficient light extraction. This has been successful for GaAs solar cells, in which good internal luminescence efficiency [6] leads to good external luminescence efficiency. (Internal luminescence efficiency is the probability of a photon to be absorbed and re-emitted, inside a solar cell.)

For GaAs, >95% internal luminescence efficiency is possible [6]. Good optical design, such as with an excellent rear mirror, can then extract those internal photons. With good external luminescence we can achieve a better voltage, as given by Miller's expression [5]:

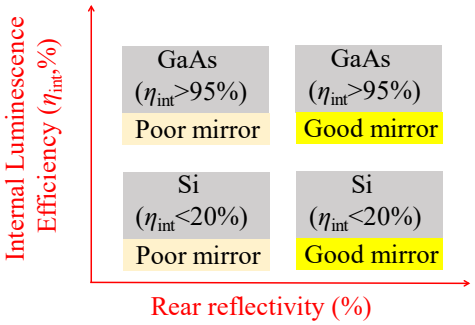

Figure 2: Relative importance of luminescence extraction. For GaAs solar cells improvement in luminescence extraction through better optical design improves V_{oc} [2, 5]. In crystalline Si, low internal luminescence efficiency hinders photo recycling and subsequent extraction. This begs the question, does textured Si offer any benefits with regards to luminescence extraction, compared to planar Si?

$$V_{\mathrm{oc}} = V_{\mathrm{oc,rad}} - \frac{kT}{q}\log\left(\frac{1}{\eta_{\mathrm{ext}}}\right) \qquad (1)$$

Here $V_{\mathrm{oc,\,rad}}$ is the voltage in the radiative limit, that is internal photons are radiated with 100% probability. T is the solar cell temperature.

On the other hand, in materials with poor η_{int} (e.g. Si), the generated electron-hole pair will be lost through non-radiative recombination, before it can be reflected from the excellent rear mirror!

Figure 1 shows the different situations for luminescence extraction in a solar cell. The vertical axis represents solar cell efficiency. GaAs with excellent η_{int} is in the top row and Si in the bottom. The horizontal axis represents the rear mirror reflectivity in the solar cell. For GaAs, an excellent rear mirror, coupled with texturing increases the luminescence extraction efficiency. This results in a significant efficiency improvement in the top right corner [5]. This is accounted for by Eq. (1).

On the bottom row, planar Si solar cells have the worst performance of all four cases. The poor luminescence severely penalizes the V_{oc}. This is also accounted for by Miller's expression in Eq. (1). Texturing and an excellent rear mirror slightly improve the efficiency for Si. This is due to increasing photon density, as proposed by Yablonovitch et. al. [X]. Voltage does not improve in this case, despite improvement in optical design. Thus Eq. (1) cannot describe the V_{oc} in the bottom right corner.

The purpose of this paper is to understand the concept of light extraction, for solar cells with poor (e.g. Si) internal luminescence efficiency. We propose a modified expression for the open-circuit voltage (V_{oc}), which applies to the case of poorly luminescent materials. Finally, we show that a minimum internal efficiency is needed before optical designs (such as an excellent rear mirror) can play a significant role in improving V_{oc} through luminescence extraction.

A Modified V_{oc} Expression:

In this section, we derive a new expression for V_{oc}. We start again from the detailed balance. For this to hold, the number of absorbed photons×η_{ext} = number of emitted photons. The absorbed photon counts can be calculated from the short-circuit current I_{sc} of the solar cell. Photon emission rate, on the other hand, can be estimated from the Shockley-Van Roosebroeck relationship [7]. Equating the two rates, we obtain (appendix for the full derivation):

$$\frac{I_{sc}}{qd} \times \eta_{ext} = Bnp \times P_{esc}$$

$$\frac{I_{sc}}{qd} \times \eta_{ext} = Bn_i^2 exp\left(\frac{qV_{oc}}{kT}\right) \times P_{esc}$$

$$V_{oc}= \frac{kT}{q}\ln\left(\frac{I_{sc}}{qdBn_i^2P_{esc}}\right)+\frac{kT}{q}\ln\left(\frac{P_{esc}\eta_{int}}{1-\eta_{int}(1-P_{loss}-P_{esc})}\right)$$

$$V_{oc}= V_{oc,ideal}+\frac{kT}{q}\ln\left(\frac{\eta_{ext}}{P_{esc}}\right) \quad (2)$$

Here, d is the thickness of the cell, B is the radiative recombination efficiency, P_{loss} is the probability that an internal photon is lost through parasitic absorption (e.g. mirror/ side-wall, etc.), and P_{esc} is the escape probability of an internal photon. In the last step, we used the multiple photon absorption and re-emission (aka photon recycling) to derive η_{ext} as follows:

$$\eta_{ext}=\eta_{int}P_{esc}+\eta_{int}P_{abs}\eta_{int}P_{esc}+...=\frac{\eta_{int}P_{esc}}{1-\eta_{int}P_{abs}}=\frac{\eta_{int}P_{esc}}{1-\eta_{int}(1-P_{loss}-P_{esc})}$$

where we use the unity probability of $P_{abs}+P_{esc}+P_{loss}=1$ in the last step. The physical processes associated with each of these probabilities are shown in Fig. (3). The ideal voltage $V_{oc,\,the\ ideal}$ is the radiative voltage in a solar cell with unity escape

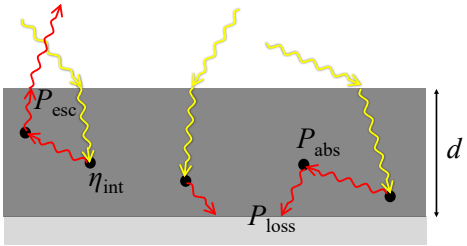

Figure 1: Photon absorption and losses inside a solar cell. The incident photon (yellow arrow) gets absorbed with a probability P_{abs}. The generated electron-hole pair recombines with a probability η_{int}. The internal photon can be lost through parasitic mechanisms, such as mirror loss (P_{loss}) or escape through the front (P_{esc}). The probabilities of each of these events depend on the thickness d of the cell.

probability.

Here, we assume non-degeneracy for the analytical derivation, $np = n_i^2\exp(\frac{qV_{oc}}{kT})$. For degenerate semiconductors, the voltage must be calculated numerically instead, and we show in the appendix that the results remain the same for both degenerate and non-degenerate cases.

The proposed V_{oc} expression in Eq. (2) conveys the complete internal physics of the solar cell, for both excellent and poor emitter materials. Let's look at the examples in Fig. (2).

First, we will show the new V_{oc} equation is applicable for materials with good η_{int}.

Let us check Eq. (2) to see if it predicts improvement of V_{oc} with better rear mirror for GaAs solar cell. In this case, 1- η_{int} (1-P_{esc}-P_{loss})≈P_{esc}+P_{loss}, since η_{int}→100%. Thus, the V_{oc} expression for high η_{int} can be approximated as:
As parasitic loss P_{loss} decreases, V_{oc} increases. Designing for efficient photon extraction thus leads to V_{oc} improvement. As such, the new V_{oc} expression indeed

$$V_{oc} = V_{oc,ideal} + \frac{kT}{q} \ln\left(\frac{\eta_{int}}{P_{loss}+P_{esc}}\right) \quad (3), \text{ for } \eta_{int} \rightarrow 100\%$$

predicts a similar dependence on luminescence extraction, as derived by Miller et. al [5].
What about materials with low η_{int}, such as crystalline Silicon?
Poor η_{int} implies internal photons are lost through non-radiative recombination even before they have a chance to escape. This is where Eq. (2) differs from the traditional V_{oc} expression from Eq. (1). In the limit of low η_{int}, we have 1- η_{int} (1-P_{esc}-P_{loss}) ≈ 1. We can use the following approximate expression for materials with poor η_{int}:

$$V_{oc} = V_{oc,ideal} + \frac{kT}{q} \ln(\eta_{int}) \quad (4), \text{ for } \eta_{int} \rightarrow 0\%$$

The new V_{oc} expression for crystalline Si in Eq. (4) is completely independent of rear mirror reflectivity! This implies designing for luminescence extraction does not necessarily improve V_{oc}. Instead, the internal luminescence needs to be good. In other words, for good external luminescence, we need good internal luminescence, to begin with.
The new V_{oc} expression given by Eq. (2) thus holds for the case of both good and poor η_{int}. It also tells us before aiming for external luminescence, we should design solar cells to have efficient internal luminescence. Indirectly, it tells us there is a minimum η_{int}, below which luminescence extraction is limited by poor η_{int}. Now the question arises, what is this minimum η_{int}? In other words, when does the new V_{oc} expression reverts to the old V_{oc} equation?

Minimum Internal Luminescence Needed for Voltage Boost:

The second term in Eq. (2) expresses the contribution of luminescence extraction on the open -circuit voltage. For materials with low internal luminescence, the second term becomes $kT/q \times \log(\eta_{int})$. We will now derive the minimum value of η_{int} for which 1- η_{int} (1-P_{esc}-P_{loss})≈1 no longer holds.
For 1- η_{int} (1-P_{esc}-P_{loss})≠1 to be true, the following condition must hold:

$$\frac{kT}{q} \log\left(\frac{\eta_{int}}{1-\eta_{int}(1-P_{loss}-P_{esc})}\right) - \frac{kT}{q} \log(\eta_{int}) \geq \frac{kT}{q}$$

Qualitatively, if the V_{oc} improvement due to luminescence extraction is less than the thermal voltage kT/q, the improvement is insignificant. With this argument, we arrive at the minimum value η_{int} as:

$$\eta_{int} \geq \frac{1 - e^{-1}}{1 - P_{loss} - P_{esc}} \qquad (5)$$

As such we can now calculate the minimum value of internal luminescence efficiency needed in a material, for V_{oc} improvement. Note that, we have not considered the effect of the optical design on I_{sc} in the first term in Eq. (2). For direct band-gap material like GaAs, this is true. For Si solar cells, texturing changes the absorptivity and as such, I_{sc} will be different for thin textured vs thin planar Si solar cells.

Now we evaluate the relevant terms in Eq. (2). We evaluate the rates P_{esc} and P_{loss} a solar cell are evaluated, similar to the expressions reported in the literature [9-12]. We assume a step-function absorptivity. We also use the material parameters for GaAs, instead of Si. Si, being indirect band-gap material, has a strong dependence of absorptivity on thickness. This dependence is not the scope of our current discussion. The derivations are provided in the appendix.

We show the effect of improving the η_{int} on the open-circuit voltage of the solar cell in Fig. 4. We also show the effect of rear mirror reflectivity R_{rear} on the same

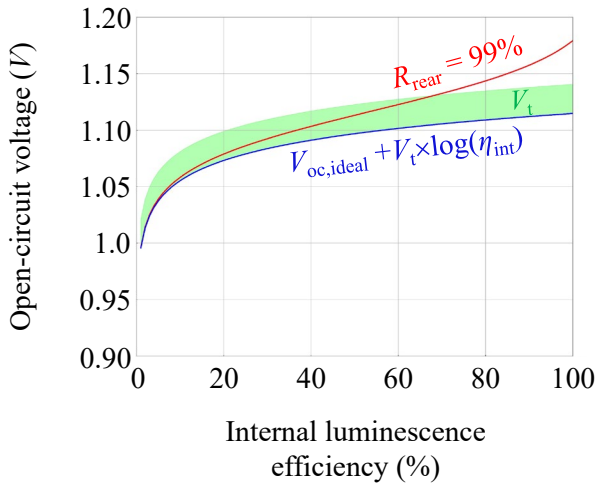

Figure 4: V_{oc} improvement through luminescence extraction. For a GaAs solar cell with 500 nm thickness and step-function absorptivity, parasitic loss decreases with improving mirror reflectivity, as shown by the red curve. However, V_{oc} improvement remains below the thermal voltage V_t (green shaded region) by mirror improvement for η_{int}<70%. Strong internal luminescence is thus necessary for a strong external luminescence, and corresponding V_{oc} improvement.

plot. A better rear mirror reduces parasitic loss. We observe that for $\eta_{int} \leq 70\%$, V_{oc} is not affected by an improvement in rear mirror reflectivity, and the voltage can be given by Eq. (2). This implies external luminescence is not strong enough to improve the V_{oc}.

We are limited by internal luminescence. Failure to luminescence internally will result in bad external luminescence. Any improvements in the optical design, by improving rear mirror reflectivity, cannot circumvent the stringent limitation due to poor η_{int}.

Thus, our new V_{oc} expression, given by Eq. (2) correctly identifies the importance of internal luminescence. The external luminescence is important for V_{oc}, but without a good internal luminescence efficiency, the design is almost irrelevant for poor luminescent solar cells! It is the internal luminescence that limits the open-circuit voltage of the solar cell with poor luminescent materials.

Conclusion:

We show that better internal luminescence efficiency is necessary for improvement in luminescence extraction in a solar cell. Strong internal luminescence can then be extracted with a good optical design. For poor emitter materials such as Si, the photons are lost internally before they can be extracted. As such, we need a minimum η_{int} in solar cells, to improve the V_{oc} through luminescence extraction. A combination of optical absorption and subsequent re-emission can push the open-circuit voltage in solar cells closer to the detailed balance limit.

References:

[1] M. A. Green, "Solar cell efficiency tables (version 56)", *Prog Photovolt*, 28 (7), 629-638, 2020.

[2] B. M. Kayes et. al., "27.6% Conversion efficiency, a new record for single-junction solar cells under 1 sun illumination," 37th IEEE PVSC, 000004-000008, 2011.

[3] W. Shockley, and H. Queisser, "Detailed Balance Limit of Efficiency of p-n Junction Solar Cells", JAP 32 (3), 510-519 (1961).

[4] R. T. Ross, "Some Thermodynamics of Photochemical Systems", *JACP* 46, 4590-4593 (1967).

[5] O. D. Miller, S. Kurtz, and E. Yablonovitch, "Strong Internal and External Luminescence as Solar Cells Approach the Shockley–Queisser Limit," IEEE Photovolt., 2(3), 303-311 (2012).

[6] M. A. Steiner et. al., "Optical enhancement of the open-circuit voltage in high-quality GaAs solar cells," JAP, 113 (12), 2013.

[7] W. Van Roosbroeck, and W. Shockley, "Photon-Radiative recombination of electrons and holes in Germanium," PRJ, 94 (6), 1954.

[8] T. Trupke, J. Zhao, A. Wang, R. Corkish, and M. A. Green, "Very efficient light emission from bulk crystalline silicon", *Appl. Phys. Lett.*, vol. 82, pp. 2996-2998, May 2003.
[9] M. A. Green et. al., "Very efficient light emission from bulk crystalline silicon", *Appl. Phys. Lett.*, vol. 82, pp. 2996-2998, May 2003.
[10] L. M. Pazos-Outon, T. P. Xiao, E. Yablonovitch, "Fundamental efficiency limit of lead iodide perovskite solar cells", *JAPCL*, 9 (7), pp. 1703-1711, March 2018.
[11] V. Ganapati, M. A. Steiner, E. Yablonovitch, "The voltage boost enabled by luminescence extraction in solar cells", IEEE Journ. Photovolt., 6 (4), pp. 801-809, March 2016.
[12] Z. Omair et. al., "Ultraefficient thermophotovoltaic power conversion by band-edge spectral filtering", PNAS, 116 (31), pp. 15356-15361, July 2019.
[13] E. Yablonovitch and G. D. Cody, "Intensity enhancement in textured optical sheets for solar cells", *IEEE Trans. Electron Devices*, vol. ED-29, no. 2, pp. 300-305, Feb. 1982.

Appendices:

Derivation of Modified V_{oc} Expression

We start our derivation from the detailed balance of photon absorption and emission. Unless otherwise stated, the symbols bear the same meaning as mentioned in the main text. In open-circuit condition,

Rate of absorbed photons per unit volume ≥ Rate of emitted photons per unit volume,

η_{ext}×Rate of absorbed photons per unit volume = Rate of emitted photons per unit volume,

η_{ext}×Rate of absorbed photons per unit volume = Rate of emitted photons per unit volume,

$\eta_{ext}\times\frac{J_{sc}}{d}$ = Rate of emitted photons per unit volume,

$\eta_{ext}\times\frac{J_{sc}}{d} = B_{ext}np$,

$\eta_{ext}\times\frac{J_{sc}}{d} = B_{ext}n_i^2\exp(\frac{qV_{oc}}{K_BT_C})$, (Assuming non-degeneracy, and B_{ext} is the external radiative recombination rate)

$\eta_{ext}\times\frac{J_{sc}}{d} = B_{int}P_{esc}n_i^2\exp(\frac{qV_{oc}}{K_BT_C})$, (Using $B_{ext} = B_{int}P_{esc}$)

$V_{oc}=\frac{kT_C}{q}\ log(\frac{J_{sc}}{B_{int}P_{esc}n_i^2 d})+\frac{kT_C}{q}\ log(\eta_{ext})$ (S1)

The first step in the derivation ensures conservation/increase of entropy. When the two rates are equal, no entropy is produced, and we have the most efficient photovoltaic absorber. But this also implies we cannot extract carriers out of the solar cell, otherwise, the two rates cannot be equal. As such, minimum entropy production in the solar cell can happen only in the open-circuit condition, when η_{ext}=1.

Now, we can use a geometric summation to derive η_{ext}. Before we do that, let's think about the definition of η_{ext}. As we use in the above definition, η_{ext} is the probability that an electron-hole pair will lead to photon emission from the solar cell. This is equivalent to the external radiative efficiency of light-emitting diodes. Now, from Fig. (S1):

$\eta_{ext}=\eta_{int}P_{esc}+\eta_{int}P_{abs}\,\eta_{int}P_{esc}+\eta_{int}P_{abs}\,\eta_{int}P_{esc}\,\eta_{int}P_{esc}+\ldots$

$\eta_{ext}=\frac{\eta_{int}P_{esc}}{1-\eta_{int}P_{abs}}=\frac{\eta_{int}P_{esc}}{1-\eta_{int}(1-P_{abs}-P_{loss})}$ (since $P_{esc}+P_{abs}+P_{loss}=1$) (S2)

The geometric sum considers the multiple absorptions and emission events encountered by a photon. This is also known as photon recycling. Replacing η_{ext} by the expression on the right in Eq. (S2), we get out modified V_{oc} expression.

Probability of Escape:

We can postulate that the photons have an ergodic distribution, inside the solar cell. This might raise questions for the case of a planar cell. However, photon recycling ensures an ergodic distribution of photons inside the solar cell, even for the planar solar cells. This can happen due to photon recycling, or diffuse reflection from the rear mirror. With this argument, we can write the escape probability P_{esc} of the photons through the solar cell as:

$$P_{esc} = \frac{\text{probability of a photon being emitted through the front surface}}{\text{probability of a photon being emitted inside the solar cell}} = \frac{\text{rate of photon emission through the front surface}}{\text{rate of internal emission of photons}} \quad \text{(S3)}$$

Now the numerator of Eq. (S3) can be evaluated as $2\pi\int_{\theta=0}^{\theta=\pi/2}\int_{E=0}^{E=\infty} a(E,\theta)b_s(E,T_c)sin(\theta)cos(\theta)\ dE\ d\theta$, where an (E, Θ) is the absorptivity of the solar cell, and $b_s(E, T_c)$ is the Planck spectrum emitted by the solar cell at temperature T_c. The denominator, on the other hand, can be estimated from the Shockley Van-Roosebroeck relationship as $\int_{E=0}^{E=\infty} 4\pi d n_s^2 \alpha(E) b_s(E,T_c)dE$, with α(E) as the absorption coefficient, d as the thickness, and n_s as the refractive index of the solar cell.

Probability of Mirror Loss:

Using a similar argument as the previous section, we can write the probability of parasitic loss in the mirror as:

$$P_{\text{loss}} = \frac{\text{probability of a photon being lost at the rear surface}}{\text{probability of a photon being emitted inside the solar cell}} = \frac{\text{rate of photon lost through the rear surface}}{\text{rate of internal emission of photons}} \quad \text{(S4)}$$

The denominator of Eq. (S4) is the same as that of Eq. (S3). For the case of the solar cell with ergodic photon distribution, $P_{\text{loss}} = n_s^2(1-R)P_{\text{esc}}$, since the photon angle randomization is equally applicable to the front and rear surfaces, except the n_s^2 modifications due to the solar cell refractive index and the factor of (1-R) from the rear mirror absorptivity.

Degenerate semiconductors:

For degenerate semiconductors, we cannot assume $np = n_i^2\exp(\frac{qV_{oc}}{k_bT_c})$.

In this case, $n = \frac{2N_c}{\sqrt{\pi}}\text{Fermi}_{1/2}(\frac{E_{FC}-E_C}{k_bT_c})$ with $\text{Fermi}_{1/2}$ as the Fermi-Dirac integral of order ½. Here E_{FC} is the electron quasi-Fermi level for electron and E_c is the conduction band-edge energy. N_c is the conduction band effective density of states. Similarly, for holes, $p = \frac{2N_c}{\sqrt{\pi}}\text{Fermi}_{1/2}(\frac{E_V-E_{FV}}{k_bT_c})$, with E_{FC}- E_{FV}= V_{oc}.

For the case of degenerate semiconductors E_C- $E_{FC} \leq \pm 3k_bT_c$, and /or E_{FV}- E_V $\leq \pm 3k_bT_c$. Using this constraint, and the relation $P_{esc}B_{int}np = \eta_{ext}I_{sc}/d$, we can solve for V_{oc} numerically for a given P_{esc}, B_{int}, η_{ext}, I_{sc}, and d. The result is shown in

Fig. S1, for R_{rear}=0% (no mirror) and R_{rear}=99%. Note that in this case, $V_{oc,\ ideal}$ cannot be directly evaluated, unlike the non-degenerate case.
We observe that a 99% reflective mirror does not improve V_{oc} more than V_t unless

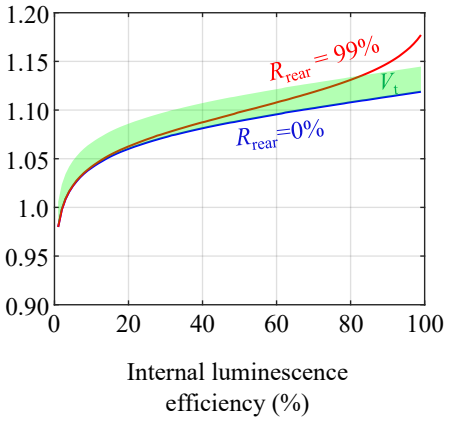

Fig. S1: V_{oc} improvement through luminescence extraction for degenerate semiconductors. For a GaAs solar cell with 500 nm thickness and step-function absorptivity, parasitic loss decreases with improving mirror reflectivity from 0% to 99%, as shown by the red curve. However, V_{oc} improvement remains below the thermal voltage V_t (green shaded region) by mirror improvement for η_{int}<82%. Strong internal luminescence is thus necessary for a strong external luminescence, and corresponding V_{oc} improvement.

η_{int}>82%. This shows that a minimum η_{int} is needed for improving V_{oc} through luminescence extraction, for both degenerate and non-degenerate semiconductors.